UNC-10/SYD-2 complex is sufficient to link kinesin-3 to RAB-3 containing synaptic vesicles in the absence of the motor's PH domain

Prerana Bhan, Odvogmed Bayansan, Chien-Yu Chang, Syed Nooruzuha Barmaver and Oliver Ingvar Wagner*

National Tsing Hua University, Institute of Molecular and Cellular Biology, Department of Life Science, Hsinchu, 30013, Taiwan (R.O.C.)

Running title: UNC-10/SYD-2 is a receptor for RAB-3 vesicles

***Corresponding author**:

Dr. Oliver I. Wagner

Professor

National Tsing Hua University

Institute of Molecular and Cellular Biology & Department of Life Science

101, Sec. 2, Kuang-Fu Road, Hsinchu 30013, Taiwan (R. O. C.)

Email: owagner@life.nthu.edu.tw

Phone: +886-3-574-2487, Fax: +886-3-571-5934

Keywords: Liprin-α, SYD-2, RIMS1, UNC-10, RAB3A, RAB-3, VAMP2, SNB-1, KIF1A, UNC-104, kinesin-3, C. elegans, BiFC, molecular motors, axonal transport, synaptic vesicles

Conflicts of interest: The authors declare no conflict of interest.

ABSTRACT

Kinesin-3 KIF1A (UNC-104 in *C. elegans*) is the major fast axonal transporter of STVs (synaptic vesicle protein transport vesicles) containing synaptic precursors such as RAB3A (RAB-3) or VAMP2 (SNB-1). Heritable mutations in neuronal motor proteins (and their adaptors) lead to numerous neurodegenerative diseases. The C-terminal PH (pleckstrin homolog) domain of kinesin-3 UNC-104 directly binds to phosphatidylinositol 4,5-bisphosphates that form the lipid bilayers of STVs. We hypothesized that RAB-3-bound STVs employ a dual linker UNC-10/SYD-2 (RIMS1/liprin-α in mammals) acting as a UNC-104 receptor. This tripartite RAB-3/UNC-10/SYD-2 complex would also act as an additional linker to strengthen the motor-lipid interaction. RT-PCR and Western blot experiments favor a genetic relation between SYD-2, UNC-10 and RAB-3. Co-immunoprecipitation assays revealed changes in binding affinities between SYD-2 and UNC-104 depending on the presence or absence of UNC-10 and RAB-3. Bimolecular fluorescence complementation (BiFC) assays revealed *in situ* interaction changes between SYD-2 and UNC-104 in either *unc-10* or *rab-3* mutants. Neuronal expression of UNC-104 appears to be more diffused and is restricted to travel short distances with significantly reduced speeds in these mutants. Though both SNB-1 and RAB-3 are actively transported by UNC-104, the movement of RAB-3 is generally enhanced and largely depending on the presence of the dual linker. Strikingly, the deletion of UNC-104's PH domain did not affect UNC-104/RAB-3 colocalization but did affect UNC-104/SNB-1 colocalization. These findings solidly support the model of a dual UNC-10/SYD-2 linker acting as a sufficient buttress to connect the motor to RAB-3-containing STVs to enhance their transport.

SCIENTIFIC STATEMENT

The interaction between molecular motors and their membranous vesicular cargoes is generally specific. However, for the major axonal transporter kinesin-3 UNC-104, only its weak and non-specific interaction via phosphatidylinositol 4,5-bisphosphates (forming the lipid bilayers of synaptic vesicles) has been characterized. Here, we present a novel, more specific way for UNC-104 to interact with synaptic vesicles - specifically with RAB-3 bound vesicles - via the dual linker complex UNC-10/SYD-2. Because many neurological diseases are linked to defects in axonal trafficking (often with protein accumulation phenotypes in neurons), understanding the molecular basis of motor/vesicle interaction might lead to the design of new drugs that may cure or prevent such diseases.

INTRODUCTION

Understanding the molecular basis of axonal transport is critical to develop novel drugs to prevent or cure various neurological diseases such as Charcot–Marie–Tooth disease (CMT), Amyotrophic lateral sclerosis (ALS) or Alzheimer's disease (1-3). The neuronal cytoskeleton is composed of microtubules (MTs), actin filaments as well as neurofilaments (NFs) all functioning to maintain neuronal polarity, morphology and integrity of axons (4-6). Axonal transport supplies axons and nerve terminals with proteins, lipids and mitochondria and prevents the build-up of misfolded proteins and toxic aggregates (7). Kinesins move from the minus-ends to plus-ends of uniformly oriented MTs in axons (anterograde transport) thereby transporting STVs (synaptic vesicle protein transport vesicles) from neuronal cell bodies (somas) to axonal termini. Retrograde transport (from the minus-ends to the plus-ends of MTs) is solely accomplished by cytoplasmic dynein (8). KIF1A is a neuron-specific molecular motor belonging to the kinesin-3 family and is termed as UNC-104 in the model organism *C. elegans*, a nematode widely used in molecular biology research. Mutations in kinesin-3 are associated to various neurological disorders including CMT, ALS and spastic paraplegia (9, 10). KIF-1A/UNC-104 is the major fast axonal transporter of synaptic vesicle precursors such as RAB-3, synaptotagmin, synaptobrevin and synaptophysin (11, 12). KIF1A-deficient mice die at the embryonic stage due to degeneration of sensory neurons based on vesicle retention in somas (13). Unusual vesicle accumulation in somas can be also observed in *C. elegans* carrying *unc-104* mutations leading to highly paralyzed worms; however these worms still survive and can be maintained in the laboratory (11). In *C. elegans*, UNC-104 associates with tau (termed PTL-1 in worms) and mutations in *ptl-1* boost SNB-1 (VAMP2) cargo movement (14). If not bound to cargo, kineins-3 motors appear monomeric and are inactivated via intramolecular folding; however, they rapidly dimerize (via their coiled coil domains) upon cargo-binding for fast and directed transport (15). Kinesin-3 motors also quickly dimerize in lipid rafts (found in vesicular surfaces) due to their ability to bind to

phosphatidylinositol 4,5-bisphosphate (PtdIns(4,5)P_2) via their PH (pleckstrin homology) domains (16).

At synapses, large electron dense structures can be seen in electron micrographs termed active zones, which are the actual sites of synaptic vesicle docking and fusion. The machinery that makes vesicle docking and fusion possible involves a variety of proteins such as MUNC-13 (UNC-13), RAB3A (RAB-3), RIMS1 (UNC-10), Liprin-α (SYD-2), CASK (LIN-2) or Clarinet (CLA-1). Direct and functional interactions between these active zone components and UNC-104 have been reported such as UNC-104/SYD-2 (17), UNC-104/RAB-3 (18), UNC-104/CLA-1 (19) and UNC-104/LIN-2 (20). SYD-2 is a multi-domain scaffolding protein that encompasses 8 N-terminal coiled coils and 3 C-terminal sterile alpha motifs (SAM domains) which are able to interact with each other to inactivate the protein via intramolecular folding (21). On the other hand, multiple SYD-2 proteins are able to form a scaffold for localized sequestering of active zone proteins (22). In *C. elegans syd-2* mutants, active zones appear diffuse and more irregular along axons causing impairment of synaptic vesicle docking, thus, synaptic transmission (23-25). The N-terminal domain of SYD-2 directly associates with other synaptic proteins such as CAST/ELKS, GIT1 and RIMS1(UNC-10) (26-30), while the C-terminal SAM domains interact with the FHA domain of UNC-104 to activate the motor (17). SYD-2/RAB-3 interactions are reported to maintain the synaptic vesicle pool at presynaptic dense projections (31).

RIMs are a family of multi-domain scaffolding proteins that were initially identified as sole Rab3-effectors to regulate synaptic vesicle fusion (32). The RIMS1 homolog in *C. elegans* is UNC-10 (33) composed of an N-terminal zinc finger motif, a central PDZ domain, two C-terminal C2 domains (C2A and C2B) and a proline-rich SH3 motif (34). RIMS1/UNC-10 interacts with multiple synaptic proteins, e.g., its N-terminal zinc finger domain interacts with GTP-bound Rab3 (32), while its C-terminal C_2B domain associates with the N-terminus of Liprin-α/SYD-2 (35). Liprin-α regulates the presynaptic organization by anchoring RIM1 and CASK to facilitate synaptic vesicle release (28) and

it has been shown that UNC-10 and SYD-2 act in the same pathway to regulate synaptic vesicle turnover (24). Based on the aforementioned direct and functional interaction between UNC-10 and SYD-2 one may speculate a role of these proteins in regulating UNC-104. We hypothesize that the UNC-10/SYD-2 complex would act to increase the specificity of UNC-104-binding to RAB-3-containing vesicles.

Rab3 is a member of the RAB family of small GTPases that recruits synaptic vesicles for vesicle docking and fusion at active zones (36). It integrates into the synaptic vesicle membrane via its C-terminal sequence Cys-X-Cys that is highly conserved in invertebrates (37). Rab3A binds to synaptic vesicles in its GTP-bound state and dissociation occurs after GTP-hydrolysis (38). The guanine nucleotide exchange factor (GEF) AEX-3 (DENN/MADD) plays an important role in regulating RAB-3, concomitantly affecting proper localization of presynaptic proteins and neurotransmitter release (39). Rab3A is transported to the active zone by the fast anterograde axonal transport system (40) and in mammals KIF1A associates to Rab3-carrying vesicles via DENN/MADD (41). Rab3A null mutant mice (36) and worms (18) display mild behavioral abnormalities, with worms specifically displaying resistance to the pesticide aldicarb. Also, synaptic transmission is perturbed in *C. elegans rab-3* mutants with a reduced amount of synaptic vesicles near the active zones (based on transport defects) (18).

Due to the characterized weak and non-specific binding between PH domains and lipid bilayers (42), and based on the aforementioned knowledge from the literature, we propose that UNC-10/SYD-2 would act as a novel receptor for UNC-104 mediated transport of RAB-3 containing vesicles. At the same time, the RAB-3/UNC-10/SYD-2 linkage would reinforce the weak motor-lipid interaction.

RESULTS

Genetic relation between *syd-2*, *unc-10* and *rab-3* in nematodes

Even though the relation between active zone proteins Liprin-α(SYD-2), RIM1(UNC-10) and Rab3A(RAB-3) has been well described in mammals as discussed above, we intend to confirm the genetic relation between SYD-2, UNC-10 and RAB-3 in nematodes. Interestingly, *syd-2* expression levels increase by 1.3~1.5 fold in *C. elegans* carrying mutations in the *unc-10* gene (investigated for two alleles *md1117* and *e102*) (Fig. 1A). The strain NM1657 *unc-10*(*md1117*) carries a large 8601 bp deletion in the unc-10 gene that includes the entire coding region along with regions of the 5' and 3' UTRs, thus likely being a knockout (Suppl. Fig. S1B) (33). Strain CB102 *unc-10*(*e102*) carries a C to T substitution in intron 15 of the *unc-10* gene resulting in splicing defects that produce a truncated protein excluding the C-terminal domain (33) (Suppl. Fig. S1B). The phenotypes of both strains NM1657 and CB102 are "mild coiler" (worm appears slightly coiled up) and "mild uncoordinated" (movements are not well directed). While SYD-2 increases in *unc-10* mutant worms, expression is decreased by about 50% in *rab-3* mutants (Fig. 1B). The strain NM791 *rab-3*(*js49*) carries a G to A transition at position 2 in the tryptophan 76 codon in the *rab-3* gene leading to a nonsense mutation causing a premature stop (18) (Suppl. Fig. S1B). The worm phenotype of NM791 is "strong coiler". Note that two other strains NM210 and NM211 exist carrying *rab-3* alone, however, these strains are poorly characterized and worm phenotypes are less pronounced (only mild uncoordinated) (wormbase.org). We also performed Western blotting from whole worm lysates and revealed that changes in syd-2 RNA expression (as shown in Fig. 1A+B) go well along with changes in respective SYD-2 protein expression (Fig. 1C+D; for representative Western blots please refer to 'Lysate' in Fig. 1E and G, respectively).

Effects of *unc-10* and *rab-3* mutations on the UNC-104/SYD-2 complex

The functional interactions between SYD-2 and UNC-104 have been well described in the literature as summarized above. To understand the role of UNC-10 and RAB-3 in this interaction scheme, we

carried out co-immunoprecipitation assays. Precipitating UNC-104::GFP (using an anti-GFP antibody) from whole worm lysates, we found that bound SYD-2 protein content was reduced in both *unc-10*(*md1117*) and *unc-10*(*e102*) mutants (Fig. 1E+F). Similarly, precipitating UNC-104::mRFP (using an anti-RFP antibody) from whole worm lysates, SYD-2 expression was significantly reduced in *rab-3*(*js49*) mutants (Fig. 1G+H). These data point to a functional relation between the UNC-104/SYD-2 complex and UNC-10 as well as RAB-3. To understand whether UNC-104/SYD-2 interactions also change in neurons of *unc-10* or *rab-3* worms, we performed colocalization as well as bimolecular fluorescence complementation (BiFC) assays. BiFC is a well- established assay in living *C. elegans* animals for investigating *in situ* functional relations between two proteins. Here, the YFP protein Venus is split into two halves (N-terminal Venus, VN, and C-terminal Venus, VC) and the test proteins are fused to each half. Complementation of Venus, leading to yellow fluorescent signals, occurs only if the two test proteins are at least 7-10 nm close to each other, therefore likely forming functional complexes (43, 44). Our data reveal that colocalization between UNC-104 and SYD-2 in nerve rings (see Suppl. Fig. 1A) significantly decreases in *unc-10*(*md1117*) and *rab-3*(*js49*) mutants as well as in *unc-10*(*md1117*) and *rab-3*(*js49*) double mutants (Fig. 2A+B). More importantly, physical interactions between UNC-104/SYD-2 complexes (as revealed by BiFC experiments) are disrupted in *unc-10*(*md1117*) and *rab-3*(*js49*) (Fig. 2C+D). These *in situ* data are consistent with our *in vitro* observations from Figure 1 and support our hypothesis that UNC-104/SYD-2 complexes are dependent on the presence of UNC-10 and RAB-3.

Role of *syd-2*, *unc-10* and *rab-3* single and double mutations on UNC-104 particle distribution in neurons

To analyze the physiological consequences of our observations, we observed changes in UNC-104 motor distributions in neurons in single (*syd-2*, *unc-10* and *rab-3*) as well as double mutants (*syd-2*/*unc-10*, *syd-2*/*rab-3*, *rab-3*/*unc-10*). In a previous study, we reported that UNC-104 forms SYD-2-dependent cluster along axons in an arrangement that does not match known *en passant* synapse

patterns, and we also demonstrated that such clusters are dynamic structures rather than inactive motor aggregates (17). In this study, we analyze UNC-104 cluster formation in the sublateral system (subdorsal and subventral neuron bundles comprised of various motor-, sensory- and inter-neurons) and a single (long) mechanosensory neuron (ALM) (Suppl. Fig. S1A). Though the focus lies in analyzing the single ALM neuron, it is evident that in both types of neurons (sublaterals and ALM) UNC-104 cluster become significantly smaller in *unc-10* and *syd-2* mutants (as well as in *rab-3* mutants when examining ALM) (Fig. 3A-C and E; Suppl. Table S1). Critically, these reductions in UNC-104 cluster sizes can be reversed to wild type levels via rescue experiments in which wild type genes are overexpressed in the respective mutants (Fig. 3E). Though double mutants did not induce clusters of even smaller sizes (as opposed to single mutants) they, on the other hand, also neither rescued nor enhanced the effects as observed in single mutants (except for *syd-2*;*unc-10* double mutant) (Fig. 3C+E). We also analyzed how far UNC-104 particles travel from the axon hillock region to distal areas of the ALM neuron (Suppl. Fig. S1C). From Figure 3D (Suppl. Table S2) it is obvious that travel distances are significantly reduced in *syd-2* mutants and that this effect can be rescued by overexpressing the wild type gene in the mutants However, such an effect cannot be seen in *rab-3* mutants, though, in *rab-3*;*unc-10* (as well as in *syd-2;unc-10* double mutants) travel distances are significantly reduced. Interestingly, in *rab-3*;*syd-2* mutants travel distances even increase (Fig. 3C+D; Suppl. Table S2) pointing to an unknown compensatory pathway. That nearly all double mutants reveal significant different effects as compared to the single mutants indicate the strong interdependences of these genes in regulating UNC-104 displacements. Especially that *rab-3* further decreases UNC-104 travel distances in *unc-10* mutants is in accordance with our model of RAB-3 being tightly linked to UNC-10. Because we assume that the reduction of UNC-104 travel distances is related to diminished motor speeds, we therefore analyzed UNC-104 motility parameters.

Role of *syd-2*, *unc-10* and *rab-3* single and double mutations on UNC-104 motility

To monitor UNC-104 motility in the long (up to 500 μm) ALM neurons, we tagged the motor's C-terminal end (Suppl. Fig. S1B) with mRFP that is reported to be less prone to self-aggregation as opposed to GFP (45). Kymograph analysis (Suppl. Fig. S1D) from recorded videos enables us to calculate various parameters such as motor velocity, total run-length, moving persistence and pausing (see Material & Methods for details). As expected from results displayed in Figure 3, all single genes *syd-2*, *unc-10* and *rab-3*, significantly reduce UNC-104 moving speeds (Fig. 4A, Suppl. Fig. S2A, Suppl. Table S3). Though run lengths remain unchanged in these genetic backgrounds, they significantly increased when overexpressing SYD-2 (Fig. 4B, Suppl. Fig. S2B, Suppl. Table S3) consistent with the literature reporting SYD-2 as an UNC-104 activator (17, 20). Furthermore, both velocities as well as motor run lengths were significantly reduced in *rab-3* double mutants *rab-3*;*unc-10* and *rab-3*;*syd-2*, yet again pointing to strong synergistic effects between these genes. Notably, low velocities and reduced run lengths in the *rab-3*;*unc-10* double mutant are consistent with observations from Figure 3C+D displaying very small travel distances for this double mutant. The parameter 'anterograde persistency' reflects the time an UNC-104 particle moves without pausing. Interestingly, these parameters behave inversely proportional to motor speeds (Fig. 4C, Suppl. Table S4), likely due to the circumstance that faster motors are more prone to lose track on microtubules as opposed to slower motors. This increased dwelling on MTs (likely due to slower speeds) goes well along with the measured reduced number of pauses (Fig. 4D). Note that we were able to successfully rescue all observed effects by overexpressing the respective wild type gene in the mutants (Fig. 4A-D). In conclusion, single and double mutant analysis point to strong synergistic effects between RAB-3, UNC-10 and SYD-2 to regulate UNC-104 motility.

UNC-10/SYD-2 complex is required for RAB-3 but not for SNB-1 based transport

Based on our hypothesis as shown in Figure 7, the UNC-10/SYD-2 complex would facilitate specific binding between the UNC-104 motor and RAB-3-containing vesicles. In this model, however, the

UNC-10/SYD-2 complex would not affect binding between motor and SNB-1-containing vesicles. Based on this assumption, we analyzed motility as well as travel distances of both mCherry::RAB-3 and SNB-1::mRFP tagged synaptic vesicles in different mutant backgrounds (Fig. 5). The UNC-104-activating effect of SYD-2 on synaptic vesicle transport (such as on RAB-3 as well as SNB-1-bound vesicles) has been well reported (17, 20) and it is not surprising that in *syd-2*(*ok217*) knockout worms speeds of both SNB-1- and RAB-3-tagged vesicles are significantly reduced (Fig. 5A+B, Suppl. Table S5). Strikingly, only speeds and run-lengths of RAB-3-bound vesicles are affected by the *unc-10*(*md1117*) allele, while SNB-1-tagged vesicles remain unaffected by the *unc-10* mutation (Fig. 5A-D, Suppl. Table 5). Similarly, *unc-10* only significantly affects travel distances of RAB-3 in ALM neurons while travels of SNB-1 vesicles remain unaffected (Fig. 5E-H, Suppl. Table S6). Interestingly, RAB-3-bound vesicles cover generally larger travel distances as compared to SNB-1-bound vesicles (Fig. 5, wild type data). As a negative control, we knocked down *rab-3* in SNB-1::mRFP expressing worms and *snb-1* in mCherry::RAB-3 expressing worms which expectedly did not affect vesicle speeds (Fig. 5A+B). In summary, these data go well along with our proposed model as shown in Figure 7.

Dual linker UNC-10/SYD-2 is sufficient to associate UNC-104 to RAB-3 bound vesicles in the absence of the motor's PH domain

Based on our proposed model as displayed in Figure 7, if eliminating UNC-104's PH domain, the motor may still effectively transport RAB-3-bound vesicles. To adequately understand whether this assumption is valid, we designed worms expressing green fluorescent UNC-104 with a deleted PH domain as well as red fluorescent RAB-3 or SNB-1. Colocalization analysis (using ICQ quantification, see Materials & Methods) revealed that UNC-104 and RAB-3 vesicles do colocalize in wild type animals even in the absence of the PH domain (Fig. 6A+B and D, Suppl. Fig. S3A+B line scans) whereas the motor does not colocalize with SNB-1 vesicles in the absence of the PH domain (Fig. 6E+F, Suppl. Fig. S4A+B line scans). This effect (SNB-1 does not colocalize with UNC-104ΔPH, but

RAB-3 does colocalize with UNC-104ΔPH) is equally evident in dorsal (Fig. 6G) and ventral (Fig. 6H) nerve cords (note that cell bodies of motor neurons are present in ventral nerve cords but not in dorsal nerve cords) (Suppl. Fig S1A). More critically, colocalization between UNC-104 and RAB-3 vesicles is significantly disrupted in *syd-2* and *unc-10* mutants (Fig. 6C+D, Suppl. Fig. S3C+D). Notably, the *unc-10* mutation does not significantly effect UNC-104/SNB-1 colocalization (Fig. 6E+F, Suppl. Fig. S4C). These data provide additional support for the model presented in Figure 7.

DISCUSSION

To capture a synaptic vesicle at the pre-synapse and to position it in a way that it perfectly opposes the neurotransmitter receptors located at the post-synapse requires a complex protein machinery. Not surprisingly, these active zones at synapses appear as dense electron structures in electron micrographs. Active zone proteins often have multiple binding partners and their multifaceted interaction sites and complex functions have been extensively studied. A key player in this protein complex is Liprin-α(SYD-2) that encompasses binding sites for KIF1A (UNC-104), RIMS1 (UNC-10), CAST, GIT, as well as the LAR (PTP-3) receptor. RIMS1 (UNC-10) itself binds to RAB3A (RAB-3), Liprin-α (SYD-2), Munc-13 (UNC-13) and CAST (46). Based on this knowledge, we propose a model in which RAB-3-containing vesicles (but not SNB-1-containing vesicles) would benefit from an additional linkage to support its binding to kinesin-3 UNC-104 (Fig. 7). This additional physical support would strengthen the well-described motor-lipid linkage (16) which is considered to be rather weak and non-specific (42). How motors bind and recognize their cargo is vividly discussed in the literature (2, 8, 9) and the dual UNC-10/SYD-2 complex may act as a novel receptor for UNC-104 to selectively transport RAB-3-containing vesicles. Our model is supported by findings that SYD-2/UNC-10, UNC-10/RAB-3 and SYD-2/RAB-3 all colocalize and are co-transported (31). Furthermore, Liprin-α(SYD-2) also affects the transport of dense-core vesicles (47) and RIM1A(UNC-10) (known to be a dense-core vesicle protein) as well as RAB-3 are all mislocalized in *liprin-α/syd-2* mutants.

Our analysis reveals a genetic linkage between unc-10 and syd-2 (Fig. 1A+B) as well as interdependencies between UNC-10 and SYD-2 to bind to UNC-104 (Fig. 1C-H). The physiological consequences of the UNC-10/SYD-2 linkage on UNC-104 neuronal particle distribution (Figs. 2+3), UNC-104 motility (Fig. 4), and UNC-104 mediated RAB-3 vesicle transport efficiencies (Figs. 5+6) are evident from this study. Indeed, it has been reported that UNC-10 acts as a stabilizer of SYD-2 in active zone complexes and that UNC-10 binding to the C-terminus of SYD-2 facilitates SYD-2's oligomerization (21, 48). The importance of oligomerized SYD-2 lies in its proposed function as a motor scaffolding protein that may bind to more than one UNC-104 at the same time (17, 21). Similarly, the functional relation between UNC-10/SYD-2 and RAB-3 is obvious from our experiments, e.g. SYD-2 binding to UNC-104 is significantly reduced in *rab-3*(*js49*) mutants (Fig. 1G+H). Moreover, the absence of *rab-3* negatively affects both UNC-104 neuronal distribution (Fig. 3E) as well as motor speeds (Fig. 4A) and these effects are significantly enhanced in the presence of *unc-10* mutations (Figs. 3D+E and 4A). UNC-104 requires *arl-8*, a small GTPase to unlock its autoinhibitory state (49). Because ARL-8 is usually associated with the cargo vesicle, it is possible that in the absence of *rab-3* not only the motor-cargo association is compromised, but also UNC-104 inactivation enhanced. Enhanced intramolecular folding of UNC-104 may then increasingly mask SYD-2 binding sites (such as SYD-2 SAM domain binding to UNC-104 FHA domain, (17, 21)) consistent with our observations from co-immunoprecipitation assays (UNC-104 binding to SYD-2 is reduced in *rab-3* mutants, Fig. 1G+H). Critically, a study that dissected the direct interactions between RAB-3 and UNC-10 in *C. elegans* suggests epistatic regulation of these proteins (50). It has been also shown that in *syd-2* mutants UNC-10 and RAB-3 mislocalize to dendrites in DA neurons (47). Furthermore, loss of *syd-2*, *unc-10* and *rab-3*, all cause depletion of synaptic vesicles at the active zones (24). To interpret measured *rab-3* effects, we also need to consider the enhancing or compensating effects by other Rabs (that may explain the partial overlapping functions of RAB-3) such as RAB-27, a close homolog of RAB-3 regulated by AEX-3 (DENN/MADD) (39, 41). On the other hand, it has been shown that various

synaptic vesicle precursors are transported in a RAB-independent fashion (41) consistent with our observations that SNB-1 is transported independently of RAB-3 and vice versa (Fig. 5A+B). More critically, we have shown that SNB-1 transport is independent of UNC-10 (Figs. 5+6). Overall slower movement of SNB-1, as opposed to RAB-3 (Fig. 5A+B, wild type data), may also be explained by the 'multiple motor model' (51) in which multiple UNC-104 motors bind to a single RAB-3 vesicle to boost transport speeds.

Visible negative effects of *unc-10* mutations on UNC-104's neuronal distributions (Fig. 3) and motor motility (Fig. 4) may lead to the notion that UNC-10 stabilizes the binding of SYD-2 to UNC-104 (Fig. 7). Loss of UNC-10 would then subsequently result in loss of SYD-2 binding leading to motor inactivation as well as reduced axonal clustering (17, 20). This notion is in accordance with observations that unc-10 RNAi even reduces observed SYD-2 overexpression effects (thus boosting motor speeds, Fig. 4A). Nevertheless, the concept of a dual UNC-10/SYD-2 linker to enhance binding specificity between UNC-104 and RAB-3-containing vesicles is only valid if deleting the motor's PH domain would not affect motor/RAB-3-vesicle interactions. Indeed, deleting the motor's PH domain does not affect the motor/RAB-3-vesicle interaction, whereas it does affect motor/SNB-1-vesicle interaction (Fig. 6). Besides the general assumption that the PH domain-binding to membranous phosphoinositides is weak (42), varying vesicular surface charges may modulate protein-lipid interactions (52). Therefore, although protein-lipid interaction seems to be imperative for UNC-104-vesicle interactions (53), both specificity and binding-strength of such interactions are generally low. Thus, the dual linker UNC-10/SYD-2 may be critical to physically strengthen motor-vesicle interactions. Moreover, because UNC-104 undergoes dimerization upon membrane-cargo binding (53, 54), such an additional linker complex may prolong the motor's activated state.

MATERIALS & METHODS

C. elegans strains and plasmids

Worms were maintained at 20°C on NGM agar plates seeded with auxotroph *E. coli* strain OP50 (as a food source) according to standard methods (55). Transgenic animals *Punc-104::unc-104::gfp*(*e1265*), *Punc-104::unc-104::mrfp*(*e1265*) and *Punc-104::unc-104::mrfp*(*ok217*) were described previously (14, 17). Strain *Punc-104::unc-104ΔPH::gfp*(*e1265*) is a kind gift from Dr. Dieter Klopfenstein (Georg-August-University, Göttingen, Germany) (see also (16)). Existing constructs *Punc-104::unc-104::gfp* and *Punc-104::unc-104::mRFP* were microinjected (using a standard protocol (56)) at a concentration of 100 ng/µl into NM1657 *unc-10*(*md1117*) and NM791 *rab-3*(*js49*) mutant worms to generate transgenic lines OIW 77 *unc-10*(*md1117*)*;nthEx77*[*Punc-104*::*unc-104::mrfp*], OIW 78 *unc-10*(*md1117*)*;nthEx78*[*Punc-104*::*unc-104::gfp*] and OIW 79 *rab-3*(*js49*)*;nthEx79*[*Punc-104*::*unc-104::mrfp*]. Note that for optimal operation of the Punc104 promoter (thus optimal UNC-104 expression) rather high injection dosages are needed (14, 17). Indeed, only unc-104 (full-length) plasmid concentrations above 70 ng/µl fully rescue the highly uncoordinated *unc-104*(*e1294*) phenotype (16). Mutant strains were received from the Caenorhabditis Genetics Center (Minnesota, USA). For colocalization studies, existing plasmid *Punc-104::gfp::syd-2* (20) was co-injected along with *Punc-104::unc-104::mrfp* (each at a concentration of 75 ng/µl) into N2 wild type animals, *unc-10*(*md1117*) and *rab-3*(*js49*) mutants animals to obtain strains OIW 80 N2;*nthEx80*[*Punc-104::gfp::syd-2;Punc-104::unc-104::mrfp*], OIW 81 *unc-10* (*md1117*);*nthEx81*[*Punc-104::gfp::syd-2;Punc-104::unc-104::mrfp*] and OIW 82 *rab-3*(*js49*);*nthEx82*[*Punc-104::gfp::syd-2;Punc-104::unc-104::mrfp*]. Likewise, *Punc-104::gfp::syd-2* (75 ng/µl) was microinjected into *unc-10*(*md1117*)*;rab-3*(*js49*)[*Punc-104::unc-104::mrfp*] to obtain OIW 83 *unc-10*(*md1117*)*,rab-3*(*js49*); *nthEx83*[*Punc-104::gfp::syd-2;Punc-104::unc-104::mrfp*]. For BiFC (bimolecular fluorescence complementation) studies, the following strains were generated using existing plasmids *Punc-104::unc-104::VC155* and *Punc-104::VN173::syd-2* (43): OIW 84 N2;*nthEx84*[*Punc-104::unc-104::VC155;Punc-*

104::VN173::syd-2], OIW 85 *unc-10*(*md1117*);*nthEx85*[*Punc-104::unc-104::VC155;Punc-104::VN173::syd-2*] and OIW 86 *rab-3*(*js49*)*;nthEx86*[*Punc-104::unc-104::VC155;Punc-104::VN173::syd-2*], respectively. For *rab-3* rescue strains, we designed a *Punc-104::rab-3::yfp* plasmid and injected it at 75 ng/µl into *rab-3*(*js49*)*;nthEx*[*Punc-104*::*unc-104::mrfp*] mutant to create OIW 87 *rab-3*(*js49*)*;nthEx87*[*Punc-104*::*unc-104::mrfp;Punc-104::rab-3::yfp*]. Likewise, *unc-10* rescue strains were generated by cloning *Punc-104::unc-10::gfp* and injecting it at 75 ng/µl into *unc-10*(*md1117*)*;nthEx*[*Punc-104*::*unc-104::mrfp*] mutant to create OIW 88 *unc-10*(*md1117*)*;nthEx88*[*Punc-104*::*unc-104::mrfp;Punc-104::unc-10::gfp*]. Similarity, *syd-2* rescue strains were obtained by co-injecting existing plasmid *Punc-104::gfp::syd-2* along with *Punc-104::unc-104::mrfp* (each at a concentration of 75 ng/µl) into *syd-2*(*ok217*) mutant worms to receive OIW 89 *syd-2*(*ok217*);*nthEx89*[*Punc-104::gfp::syd-2;Punc-104::unc-104::mrfp*]. *Punc-104::mcherry::rab-3* was designed by amplifying the rab-3 gene from cDNA libraries using primers ATGGCGGCTGGCGGACAA (forward) and TTAGCAATTGCATTGCTGTT (reverse). In order to generate transgenic lines expressing cargo markers, we injected existing constructs *Punc-86::snb-1::mRFP* (17) and *Punc-104::mcherry::rab-3* into N2 wild type animals, *unc-10*(*md1117*) and *syd-2*(*ok217*) mutants (at 100 ng/µl) to obtain strains OIW 90 N2;*nthEx90*[*Punc-86::snb-1::mRFP*], OIW 91 N2;*nthEx91*[*Punc-104::mcherry::rab-3*], OIW 92 *syd-2*(*ok217*)*;nthEx92*[*Punc-86::snb-1::mRFP*], OIW 93 *syd-2*(*ok217*)*;nthEx93*[*Punc-104::mcherry::rab-3*], OIW 94 *unc-10*(*md1117*)*;nthEx94*[*Punc-86::snb-1::mRFP*] and OIW 95 *unc-10*(*md1117*)*;nthEx95*[*Punc-104::mcherry::rab-3*]. For UNC-104 and RAB-3 colocalization studies, plasmids *Punc-104::unc-104ΔPH::gfp* and *Punc-104::mcherry::rab-3* were coinjected into N2 wild type animals, *unc-10*(*md1117*) and *syd-2*(*ok217*) mutants to generate OIW 96 N2;*nthEx96*[*Punc-104::unc-104ΔPH::gfp;Punc-104::mcherry::rab-3*], OIW 97 *unc-10*(*md1117*);*nthEx97*[*Punc-104::unc-104ΔPH::gfp;Punc-104::mcherry::rab-3*] and OIW 98 *syd-2*(*ok217*)*;nthEx98*[*Punc-104::unc-104ΔPH::gfp;Punc-104::mcherry::rab-3*]. For BiFC experiments *Punc-104::rab-3::VN173* and

Punc-104::snb-1::VC155 plasmids were generated by amplifying *rab-3* cDNA using primers GGCGCGCCATGAATAATCAACAGGC (forward) with an AscI site and ACCGGTGCAATTGCATTGCTGTTGAG (reverse) with an AgeI site and substituted a *map-1* insert in *Punc-104::map-1::VN173* (20) with *rab-3*. Similarly, *snb-1* genomic DNA was amplified using primers GGCGCGCCATGGACGCTCAAGGAGATGC (forward) with an AscI site and GGTACCTTTTCCTCCAGCCCATAAAACGATGA (reverse) with a KpnI site and substituted *lin-2* in *Punc-104::lin-2::VC155* (20) with *snb-1*. These plasmids were then co-injected (80 ng/µl) into N2 worms to generate OIW 99 N2;*nthEx99*[*Punc-104::rab-3::VN173;Punc-104::snb-1::VC155*]. Lastly, *unc-10*(*md1117*)*;rab-3*(*js49*) double mutant was generated by crossing *unc-10* (*md1117*)*;nthEx*[*Punc-104*::*unc-104::mrfp*] expressing male worms with *rab-3*(*js49*) hermaphrodites. Red fluorescent males from the F_1 generation exhibiting coiler phenotypes were back-crossed into *rab-3*(*js49*) F_0 hermaphrodites to obtain *unc-10*(*md1117*)*;rab-3*(*js49*) homozygous animals.

Real-time PCR

To evaluate *syd-2* RNA levels in lysates from *unc-10* and *rab-3* mutant worms (Fig. 1A+B), we performed Real-Time PCR assays employing an ABI StepOnePlus Real-Time PCR machine in conjunction with the ABI Power SYBR green PCR master mix. Worms lysates are prepared from young adults based on a previously described protocol (57). RNA levels of *syd-2* were normalized to the *cdc-42* gene that acts as an internal control. The following primers were used: CGGAACAATACTCGACTTC (forward) and GCCACACGCTCCATT (reverse) that includes a part of 2nd and 4th exon (200 bp) for *syd-2* and CTGCTGGACAGGAAGATTACG (forward) and TCGGACATTCTCGAATGAAG (reverse) for *cdc-42.*

RNAi feeding assay

For RNA interference experiments, we employed the RNAi feeding method (58) in which worms are fed by bacteria producing the desired dsRNA. We obtained feeding clones UNC-10(X-3F06), SYD-2(X-5K09) and SNB-1 (V-4J14) from the Julie Ahringer's *C. elegans* RNAi feeding library (Source

BioScience LifeSciences, USA; a kind gift of the *C. elegans* Core Facility, Taiwan) which we sequenced to determine their correctness. NGM plates containing ampicillin (25 µg/ml) and 1 mM IPTG were inoculated with the respective HT115 *E. coli* strain carrying the appropriate gene insert (flanked by T7 promoters) and grown overnight. Fifteen to twenty worms were transferred to the respective RNAi feeding plate and incubated at 20˚C. Worms were then transferred to new RNAi feeding plates every 24 hours and the F1 progeny was used for analysis after day 5.

Western blotting and co-immunoprecipitation assays

To extract proteins from worms, we prepared lysates from young adults based on a previously described protocol (57). To perform Western blots from whole worm lysates, 100 µg sample protein was used and membrane blocking was carried out using milk powder for 1-1.5 hours at RT. Primary goat (N-terminal) anti-SYD-2 antibody (cL-19 #sc-15655, Santa Cruz) was incubated at 4°C for 14 hours at 1/500 dilutions. Secondary anti-goat antibody was incubated at RT for 2 hours with 1/1000 dilutions. Anti β-actin antibody was used as loading control (sc-47778, Santa Cruz). For Co-IPs, we use the PureProteome Protein G Magnetic Bead System (EMD Millipore Corp.). 1 mg protein extract was used for immunoprecipitation and incubated with protein G beads and 4 µg mouse anti-GFP antibody (B-2 #sc-9996, Santa Cruz). Western blotting (Fig. 1E-H) was performed using a 1:500 dilution of the anti-SYD-2 antibody (primary antibodies dilutions based on the manufacturer's suggestion). Band density analysis was carried out using NIH ImageJ 1.50 software based on a published protocol (59).

Worm imaging and motility analysis

For microscopic observations, worms were immobilized on 2% agarose-coated cover slides, and no anesthetics (e.g., levamisole) were used (reported to affect motor motility (60)). A Zeiss LSM780 confocal laser scanning microscope was employed for imaging worms as shown in Figures 2 and 6. For motility analysis (Fig. 4) and further imaging (Figs. 3 and 5), we employed an Olympus IX81 microscope with a DSU Nipkow spinning disk unit connected to an Andor iXon DV897 EMCCD

camera for high-speed and long-duration time-lapse imaging (4-5 frames per second). To convert recorded time-lapse sequences into kymographs, we used imaging analysis software NIH ImageJ. The 'straighten plugin' was used to straighten curved axons, and after drawing a line over the axon, the plugin 'reslice stack function' was executed to generate kymographs. In kymographs, static particles appear as vertical lines, whereas the slope of a moving particle corresponds to the velocity (speed) of the particle. A pause is defined if motors move less than 0.07 µm/s, and each calculated velocity event does not contain any pauses. On average, we analyzed approximately 600 moving events per experiment from 15 to 25 individual worms. A moving event is defined as a single motility occurrence typically right after a pause or a reversal, and an event ends when the motor again pauses or reverses. Motor cluster analysis (Fig. 3B+E) was carried out using ImageJ's 'area' tool and the 'particle analyze' plugin. To measure travel distances (Figs. 3D and 5F+H) of particles in (straightened) neurons, we used ImageJ's 'line tool' to draw a line from the proximal axon hillock to the identified distal particle. Intensity Correlation Quotient (ICQ) (Figs. 2B and 6D+F) was measured by selecting the region of interest using the 'polygonal selection tool' in ImageJ. After background fluorescent intensity subtraction (ImageJ 'Subtract Background' function), the plugin 'Intensity Correlation Analysis' was used to generate ICQ values. ICQ values range from -0.5 to 0.5, and values close to 0.5 stand for interdependent expression of two fluorophores while values close to -0.5 stand for segregated expression, and values around 0 imply random expression. For fluorescence intensity quantification (Fig. 2D), the following formula was used: 'Integrated density of selected region – (area of selected region * mean fluorescence of the background)' (61). Parameters such as mean grey value of background, area of selected region and integrated density of selected region were determined using ImageJ's region selection tools. Line scans (Suppl. Figs. S3 and S4) were generated using ImageJ 'Plot profile' function after straightening the neurite using ImageJ's 'straighten' tool.

ACKNOWLEDGEMENTS

We thank the *C. elegans* Core Facility (CECF) Taiwan (funded by the Ministry of Science and Technology, MOST) for providing microinjection setups and worm observation systems. We acknowledge MOST grant NSC 100-2311-B-007-004 to OIW and support from the Brain Research Center of National Tsing Hua University under the Higher Education Sprout Project funded by the Ministry of Science and Technology and Ministry of Education in Taiwan.

REFERENCES

1. B. R. Brooks, The role of axonal transport in neurodegenerative disease spread: a meta-analysis of experimental and clinical poliomyelitis compares with amyotrophic lateral sclerosis. *Can J Neurol Sci* **18**, 435-438 (1991).
2. M. A. Franker, C. C. Hoogenraad, Microtubule-based transport - basic mechanisms, traffic rules and role in neurological pathogenesis. *J Cell Sci* **126**, 2319-2329 (2013).
3. M. Breuss, D. A. Keays, Microtubules and neurodevelopmental disease: the movers and the makers. *Adv Exp Med Biol* **800**, 75-96 (2014).
4. L. Luo, Actin cytoskeleton regulation in neuronal morphogenesis and structural plasticity. *Annu Rev Cell Dev Biol* **18**, 601-635 (2002).
5. A. P. Barnes, F. Polleux, Establishment of axon-dendrite polarity in developing neurons. *Annu Rev Neurosci* **32**, 347-381 (2009).
6. L. C. Kapitein, C. C. Hoogenraad, Which way to go? Cytoskeletal organization and polarized transport in neurons. *Mol Cell Neurosci* **46**, 9-20 (2011).
7. E. Perlson, S. Maday, M. M. Fu, A. J. Moughamian, E. L. Holzbaur, Retrograde axonal transport: pathways to cell death? *Trends Neurosci* **33**, 335-344 (2010).
8. S. Maday, A. E. Twelvetrees, A. J. Moughamian, E. L. Holzbaur, Axonal Transport: Cargo-Specific Mechanisms of Motility and Regulation. *Neuron* **84**, 292-309 (2014).

9. S. T. Brady, G. A. Morfini, Regulation of motor proteins, axonal transport deficits and adult-onset neurodegenerative diseases. *Neurobiol Dis* **105**, 273-282 (2017).

10. S. Millecamps, J. P. Julien, Axonal transport deficits and neurodegenerative diseases. *Nat Rev Neurosci* **14**, 161-176 (2013).

11. D. H. Hall, E. M. Hedgecock, Kinesin-related gene unc-104 is required for axonal transport of synaptic vesicles in C. elegans. *Cell* **65**, 837-847 (1991).

12. C. I. Maeder, A. San-Miguel, E. Y. Wu, H. Lu, K. Shen, In vivo neuron-wide analysis of synaptic vesicle precursor trafficking. *Traffic* **15**, 273-291 (2014).

13. Y. Yonekawa *et al.*, Defect in synaptic vesicle precursor transport and neuronal cell death in KIF1A motor protein-deficient mice. *J Cell Biol* **141**, 431-441 (1998).

14. N. W. Tien, G. H. Wu, C. C. Hsu, C. Y. Chang, O. I. Wagner, Tau/PTL-1 associates with kinesin-3 KIF1A/UNC-104 and affects the motor's motility characteristics in C. elegans neurons. *Neurobiol Dis* **43**, 495-506 (2011).

15. D. J. Rashid, J. Bononi, B. P. Tripet, R. S. Hodges, D. W. Pierce, Monomeric and dimeric states exhibited by the kinesin-related motor protein KIF1A. *J Pept Res* **65**, 538-549 (2005).

16. D. R. Klopfenstein, R. D. Vale, The lipid binding pleckstrin homology domain in UNC-104 kinesin is necessary for synaptic vesicle transport in Caenorhabditis elegans. *Mol Biol Cell* **15**, 3729-3739 (2004).

17. O. I. Wagner *et al.*, Synaptic scaffolding protein SYD-2 clusters and activates kinesin-3 UNC-104 in C. elegans. *Proc Natl Acad Sci U S A* **106**, 19605-19610 (2009).

18. M. L. Nonet *et al.*, Caenorhabditis elegans rab-3 mutant synapses exhibit impaired function and are partially depleted of vesicles. *J Neurosci* **17**, 8061-8073 (1997).

19. Z. Xuan *et al.*, Clarinet (CLA-1), a novel active zone protein required for synaptic vesicle clustering and release. *Elife* **6** (2017).

20. G. H. Wu, M. Muthaiyan Shanmugam, P. Bhan, Y. H. Huang, O. I. Wagner, Identification and Characterization of LIN-2(CASK) as a Regulator of Kinesin-3 UNC-104(KIF1A) Motility and Clustering in Neurons. *Traffic* **17**, 891-907 (2016).
21. P. H. Chia, M. R. Patel, O. I. Wagner, D. R. Klopfenstein, K. Shen, Intramolecular regulation of presynaptic scaffold protein SYD-2/liprin-alpha. *Mol Cell Neurosci* **56**, 76-84 (2013).
22. S. A. Spangler, C. C. Hoogenraad, Liprin-alpha proteins: scaffold molecules for synapse maturation. *Biochem Soc Trans* **35**, 1278-1282 (2007).
23. M. Zhen, Y. Jin, The liprin protein SYD-2 regulates the differentiation of presynaptic termini in C. elegans. *Nature* **401**, 371-375 (1999).
24. C. Stigloher, H. Zhan, M. Zhen, J. Richmond, J. L. Bessereau, The presynaptic dense projection of the Caenorhabditis elegans cholinergic neuromuscular junction localizes synaptic vesicles at the active zone through SYD-2/liprin and UNC-10/RIM-dependent interactions. *J Neurosci* **31**, 4388-4396 (2011).
25. M. Kittelmann *et al.*, Liprin-alpha/SYD-2 determines the size of dense projections in presynaptic active zones in C. elegans. *J Cell Biol* **203**, 849-863 (2013).
26. F. Ackermann, C. L. Waites, C. C. Garner, Presynaptic active zones in invertebrates and vertebrates. *EMBO Rep* **16**, 923-938 (2015).
27. H. Shin *et al.*, Association of the kinesin motor KIF1A with the multimodular protein liprin-alpha. *J Biol Chem* **278**, 11393-11401 (2003).
28. S. A. Spangler *et al.*, Liprin-alpha2 promotes the presynaptic recruitment and turnover of RIM1/CASK to facilitate synaptic transmission. *J Cell Biol* **201**, 915-928 (2013).
29. Y. Dai *et al.*, SYD-2 Liprin-alpha organizes presynaptic active zone formation through ELKS. *Nat Neurosci* **9**, 1479-1487 (2006).
30. J. Ko *et al.*, Interaction between liprin-alpha and GIT1 is required for AMPA receptor targeting. *J Neurosci* **23**, 1667-1677 (2003).

31. Y. E. Wu, L. Huo, C. I. Maeder, W. Feng, K. Shen, The balance between capture and dissociation of presynaptic proteins controls the spatial distribution of synapses. *Neuron* **78**, 994-1011 (2013).

32. Y. Wang, M. Okamoto, F. Schmitz, K. Hofmann, T. C. Sudhof, Rim is a putative Rab3 effector in regulating synaptic-vesicle fusion. *Nature* **388**, 593-598 (1997).

33. S. P. Koushika *et al.*, A post-docking role for active zone protein Rim. *Nat Neurosci* **4**, 997-1005 (2001).

34. Y. Wang, S. Sugita, T. C. Sudhof, The RIM/NIM family of neuronal C2 domain proteins. Interactions with Rab3 and a new class of Src homology 3 domain proteins. *J Biol Chem* **275**, 20033-20044 (2000).

35. S. Schoch *et al.*, RIM1alpha forms a protein scaffold for regulating neurotransmitter release at the active zone. *Nature* **415**, 321-326 (2002).

36. M. Geppert *et al.*, The role of Rab3A in neurotransmitter release. *Nature* **369**, 493-497 (1994).

37. P. A. Johnston *et al.*, rab3A attachment to the synaptic vesicle membrane mediated by a conserved polyisoprenylated carboxy-terminal sequence. *Neuron* **7**, 101-109 (1991).

38. G. Fischer von Mollard, B. Stahl, C. Li, T. C. Sudhof, R. Jahn, Rab proteins in regulated exocytosis. *Trends Biochem Sci* **19**, 164-168 (1994).

39. T. R. Mahoney *et al.*, Regulation of synaptic transmission by RAB-3 and RAB-27 in Caenorhabditis elegans. *Mol Biol Cell* **17**, 2617-2625 (2006).

40. J. Y. Li, R. Jahn, A. Dahlstrom, Rab3a, a small GTP-binding protein, undergoes fast anterograde transport but not retrograde transport in neurons. *Eur J Cell Biol* **67**, 297-307 (1995).

41. S. Niwa, Y. Tanaka, N. Hirokawa, KIF1Bbeta- and KIF1A-mediated axonal transport of presynaptic regulator Rab3 occurs in a GTP-dependent manner through DENN/MADD. *Nat Cell Biol* **10**, 1269-1279 (2008).

42. M. A. Lemmon, K. M. Ferguson, Molecular determinants in pleckstrin homology domains that allow specific recognition of phosphoinositides. *Biochem Soc Trans* **29**, 377-384 (2001).

43. C. C. Hsu, J. D. Moncaleano, O. I. Wagner, Sub-cellular distribution of UNC-104(KIF1A) upon binding to adaptors as UNC-16(JIP3), DNC-1(DCTN1/Glued) and SYD-2(Liprin-alpha) in C. elegans neurons. *Neuroscience* **176**, 39-52 (2011).

44. C. D. Hu, T. K. Kerppola, Simultaneous visualization of multiple protein interactions in living cells using multicolor fluorescence complementation analysis. *Nat Biotechnol* **21**, 539-545 (2003).

45. R. E. Campbell *et al.*, A monomeric red fluorescent protein. *Proc Natl Acad Sci U S A* **99**, 7877-7882 (2002).

46. M. Zhen, Y. Jin, Presynaptic terminal differentiation: transport and assembly. *Curr Opin Neurobiol* **14**, 280-287 (2004).

47. P. R. Goodwin, P. Juo, The scaffolding protein SYD-2/Liprin-alpha regulates the mobility and polarized distribution of dense-core vesicles in C. elegans motor neurons. *PloS one* **8**, e54763 (2013).

48. H. Taru, Y. Jin, The Liprin homology domain is essential for the homomeric interaction of SYD-2/Liprin-alpha protein in presynaptic assembly. *J Neurosci* **31**, 16261-16268 (2011).

49. S. Niwa *et al.*, Autoinhibition of a Neuronal Kinesin UNC-104/KIF1A Regulates the Size and Density of Synapses. *Cell Rep* **16**, 2129-2141 (2016).

50. E. O. Gracheva, G. Hadwiger, M. L. Nonet, J. E. Richmond, Direct interactions between C. elegans RAB-3 and Rim provide a mechanism to target vesicles to the presynaptic density. *Neurosci Lett* **444**, 137-142 (2008).

51. M. Vershinin, B. C. Carter, D. S. Razafsky, S. J. King, S. P. Gross, Multiple-motor based transport and its regulation by Tau. *Proc Natl Acad Sci U S A* **104**, 87-92 (2007).

52. J. L. Richens, J. S. Lane, J. P. Bramble, P. O'Shea, The electrical interplay between proteins and lipids in membranes. *Biochim Biophys Acta* **1848**, 1828-1836 (2015).

53. D. R. Klopfenstein, M. Tomishige, N. Stuurman, R. D. Vale, Role of phosphatidylinositol(4,5)bisphosphate organization in membrane transport by the Unc104 kinesin motor. *Cell* **109**, 347-358 (2002).

54. M. Tomishige, D. R. Klopfenstein, R. D. Vale, Conversion of Unc104/KIF1A kinesin into a processive motor after dimerization. *Science* **297**, 2263-2267 (2002).

55. S. Brenner, The genetics of Caenorhabditis elegans. *Genetics* **77**, 71-94 (1974).

56. C. C. Mello, J. M. Kramer, D. Stinchcomb, V. Ambros, Efficient gene transfer in C.elegans: extrachromosomal maintenance and integration of transforming sequences. *EMBO J* **10**, 3959-3970 (1991).

57. S. Ward *et al.*, Genomic organization of major sperm protein genes and pseudogenes in the nematode Caenorhabditis elegans. *Journal of molecular biology* **199**, 1-13 (1988).

58. R. S. Kamath, M. Martinez-Campos, P. Zipperlen, A. G. Fraser, J. Ahringer, Effectiveness of specific RNA-mediated interference through ingested double-stranded RNA in Caenorhabditis elegans. *Genome Biol* **2**, RESEARCH0002 (2001).

59. C. A. Schneider, W. S. Rasband, K. W. Eliceiri, NIH Image to ImageJ: 25 years of image analysis. *Nature methods* **9**, 671-675 (2012).

60. J. Kumar *et al.*, The Caenorhabditis elegans Kinesin-3 motor UNC-104/KIF1A is degraded upon loss of specific binding to cargo. *PLoS Genet* **6**, e1001200 (2010).

61. Q. Li *et al.*, A syntaxin 1, Galpha(o), and N-type calcium channel complex at a presynaptic nerve terminal: analysis by quantitative immunocolocalization. *J Neurosci* **24**, 4070-4081 (2004).

FIGURE LEGENDS

Figure 1: Real-Time PCR and co-immunoprecipitation assays to investigate genetic and functional relations between syd-2, unc-10 and rab-3 in *C. elegans*. (A+B) Relative syd-2 RNA expression levels in different *unc-10* (A) and *rab-3* (B) allelic backgrounds. RNA levels normalized to endogenous cdc-42 expression as an internal control. (C) SYD-2 protein expression changes in different *unc-10* (A) and *rab-3* (B) allelic backgrounds. Data revealed from Western blot band intensity measurements and representative Western blot examples shown in (E, 'Lysate') and (G, 'Lysate'). (E) Immunoprecipitation of UNC-104 and detection of bound SYD-2 (using an anti-SYD-2 antibody) in lysates from worms expressing UNC-104::GFP either in wild type or in two different *unc-10* allelic backgrounds. (F) Quantification of data from Western blots (representative gel in (E, 'Lysate')). (H) Quantification of data from Western blots (representative gel in (G, 'Lysate')). SYD-2 band signal intensities in each sample is normalized against IgG. (A), (C) and (F): One-way ANOVA with Dunnett's test for multiple comparisons with ** $p<0.005$, *** $p< 0.001$, **** $p<0.0001$. (B), (D) and (H): Two-tailed, unpaired Student's t-test with ***$p<0.001$, ****$p<0.0001$. Box and whisker graphs represent maximum value, upper quartile, median, lower quartile and minimum value. No of trials for each experimental group = 3.

Figure 2: Colocalization and bimolecular fluorescence complementation assays (BiFC) between UNC-104 and SYD-2 in the presence or absence of *unc-10* or *rab-3*. (A) UNC-104 and SYD-2 colocalization in the nerve ring (see Suppl. Fig. S1A) of wild type, *unc-10*, *rab-3*, and *unc-10;rab-3* worms. White arrows highlight exemplified colocalization events. (B) Intensity correlation coefficients from images shown in (A) (n = 20 worms). (C) UNC-104 and SYD-2 BiFC signals in the nerve ring of wild type, *unc-10* and *rab-3* worms. UNC-104/UNC-104 BiFC used as positive and UNC-104/empty (empty vector) used as negative BiFC control. White dashed lines designate the borders of the worm's head (see Suppl. Fig. S1A). (D) Fluorescence intensity measurements from images shown in (C) (n = 25 worms). A = anterior, P = posterior directions (in (C)). One-way ANOVA

with Dunnett's test for multiple comparisons was used with **** p<0.0001. Box and whisker graphs represent maximum value, upper quartile, median, lower quartile and minimum value. Scale bar: 10 µm.

Figure 3: Effect of *syd-2*, *unc-10* and *rab-3* single and double mutations on UNC-104 clustering in sublateral nerve bundles and single ALM neurons. (A) UNC-104 cluster patterning in sublateral (see Suppl. Fig. 1A) nerve bundles. (B) Cluster size (area) quantification from (A). (C) Stacks of ALM (see Suppl. Fig. 1A) neurons (after digital straightening) reflect characteristic UNC-104 cluster patterning in different mutants. (D) Quantification of average distances travelled from the axonal hillock (red dotted line in (C)) to distal areas in the neuron (data taken from (C)) (see Suppl. Fig. 1C). (E) Cluster size (area) quantification from (C). One-way ANOVA with Dunnett's test for multiple comparisons was used with * p<0.05, ** p<0.005, *** p< 0.001, **** p<0.0001. For comparisons of means of two groups in (D) we used two-tailed, unpaired Student's t-test with ****p<0.0001. Box and whisker graphs represent maximum value, upper quartile, median, lower quartile and minimum value. N = 20 worms per experimental group. Further details of data can be found in in Suppl. Tables S1+2. Scale bar: 10 µm.

Figure 4: Effect of *syd-2*, *unc-10* and *rab-3* single and double mutations on kinesin-3 UNC-104 motility in neurons of living *C. elegans* animals. (A) Anterograde velocity of UNC-104 in *syd-2, unc-10, rab-3* single mutants as well as in various double mutant combinations. Green dotted lines outline particular data set comparisons. (B) UNC-104 anterograde run lengths. For frequency distribution profiles (histograms) refer to Suppl. Fig. S2. Red wild cards indicate t-tests between *unc-10* and *unc-10;rab-3* double mutants. (C) Anterograde moving persistency of UNC-104. (D) UNC-104 pausing behavior. Red wild cards indicate t-tests between *unc-10* and *unc-10;rab-3* double mutants. Analyzed total events: UNC-104(wt) = 689, *syd-2*(*ok217*) = 535, *unc-10*(*md1117*) = 515, *rab-3*(*js49*) = 520, *unc-10;rab-3* = 522, *syd-2*(*ok217*)*;unc-10* RNAi = 536, r*ab-3*(*js49*)*;syd-2* RNAi = 518, *rab-3* rescue = 535, *syd-2* rescue = 323, *unc-10* rescue = 495, *syd-2* overexpression = 595, *syd-2*

overexpression*;unc-10* RNAi = 570. One-way ANOVA with Dunnett's test for multiple comparisons was used with * p<0.05, ** p<0.005, *** p< 0.001, **** p<0.0001. For comparisons of means of two groups in (A+B) and (D) we used two-tailed, unpaired Student's t-test with **p<0.01, ***p<0.001, ****p<0.0001. Box and whisker graphs represent maximum value, upper quartile, median, lower quartile and minimum value. Further details of data can be found in in Suppl. Tables S3-5.

Figure 5: Effect of *syd-2*, *unc-10* and *rab-3* single and double mutations on SNB-1 and RAB-3 cargo trafficking. (A) Anterograde velocities of SNB-1-tagged synaptic vesicles. (B) Anterograde velocities of RAB-3-tagged synaptic vesicles. (C) Anterograde run lengths of SNB-1-tagged synaptic vesicles. (D) Anterograde run lengths of RAB-3-tagged synaptic vesicles. (E) Stacks of ALM neurons unravels characteristic SNB-1 cluster patterning in different mutants. (F) Quantification of average distances travelled from the axonal hillock (red dotted line in (E)) to distal areas in the neuron (data taken from (E); n = 20 worms). (G) Stacks of ALM neurons to demonstrate RAB-3 cluster patterning in different mutants. (H) Quantification of average distances travelled from the axonal hillock (red dotted line in (G)) to distal areas in the neuron (data taken from (G); n = 20 worms). Further details of data can be found in in Suppl. Tables S6. Analyzed total moving events in (A-D): SNB-1(wt) = 510, *rab-3* RNAi = 360, *syd-2*(*ok217*) = 439, *unc-10*(*md1117*) = 518, *unc-10*(*md1117*)*;syd-2* RNAi = 250, RAB-3(wt) = 513, *snb-1* RNAi = 306, *syd-2*(*ok217*) = 508, *unc-10*(*md1117*) = 509 and *unc-10*(*md1117*)*;syd-2* RNAi = 300. One-way ANOVA with Dunnett's test for multiple comparisons was used with * p<0.05, ** p<0.005, *** p< 0.001, **** p<0.0001. Box and whisker graphs represent maximum value, upper quartile, median, lower quartile and minimum value. Scale bar: 10 µm.

Figure 6: Interaction between RAB-3/UNC-104 and SNB-1/UNC-104 in the presence or absence of the motor's PH domain. RAB-3 colocalization with (A) full length UNC-104 and (B) with UNC-104 lacking the PH domain (UNC-104ΔPH). (C) Colocalization of UNC-104ΔPH and RAB-3 in *syd-2* and *unc-10* knockout worms. (D) Quantification of data from (A-C). For line scans along neurites refer to Suppl. Fig. S3. (E) SNB-1 colocalization with full length UNC-104 (wt and *unc-10* mutant) as

well as with UNC-104 lacking the PH domain. (F) Quantification of data from (E). (G-H) Colocalization of UNC-104ΔPH/SNB-1 and UNC-104ΔPH/RAB-3 in dorsal and ventral nerve cords. One-way ANOVA with Dunnett's test for multiple comparisons was used with ** $p<0.005$, *** $p<0.001$, **** $p<0.0001$. Box and whisker graphs represent maximum value, upper quartile, median, lower quartile and minimum value. N = 20 worms for all experimental groups. Scale bar: 10 µm.

Figure 7: Model of an UNC-10/SYD-2 receptor in UNC-104-mediated RAB-3 cargo transport. (A) Current model of weak and unspecific UNC-104-vesicle interactions. (B) Presence of UNC-10/SYD-2 receptor promotes RAB-3 cargo transport.

FIGURES

FIGURE 1

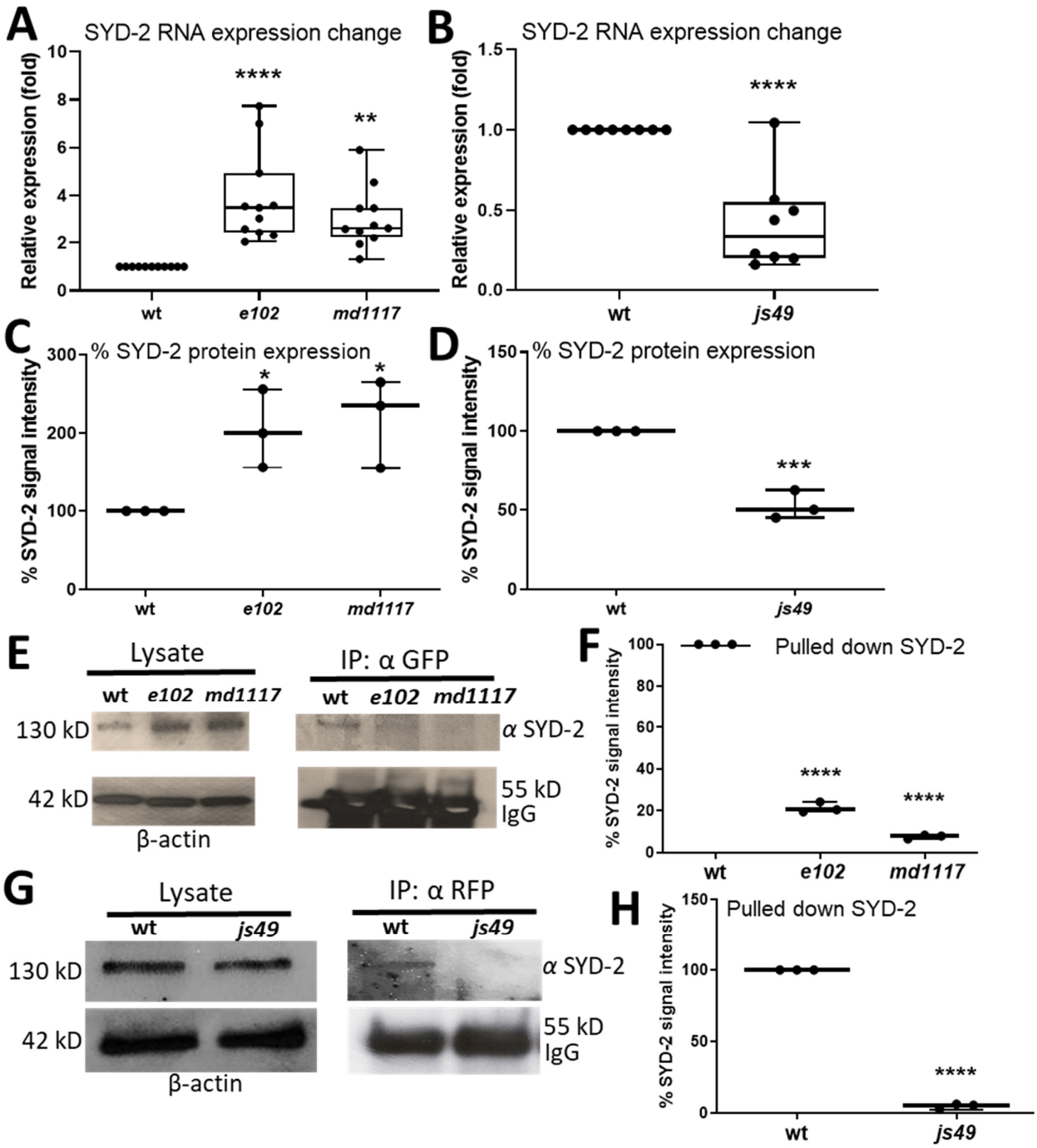

FIGURE 2

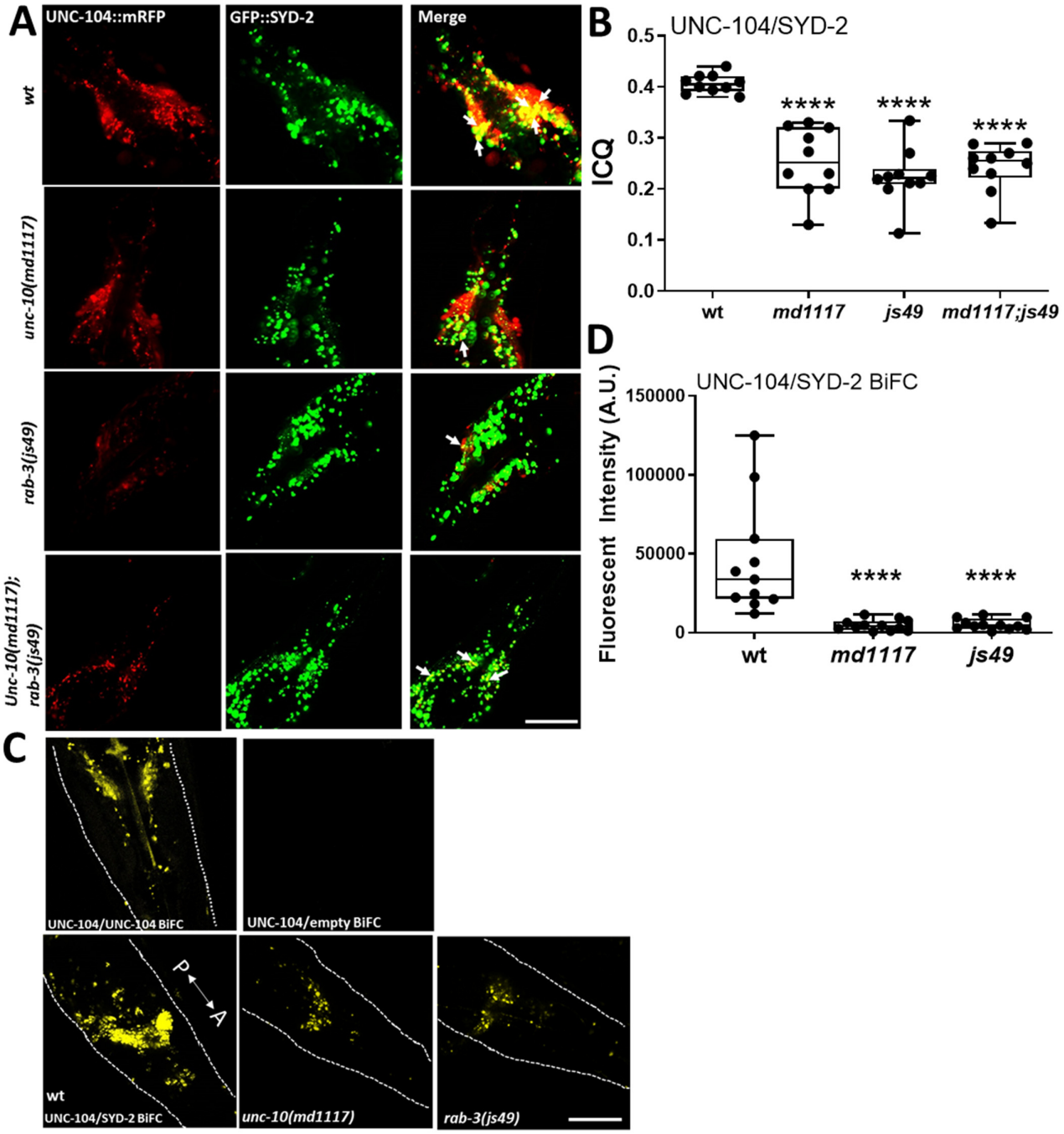
A
UNC-104::mRFP
GFP::SYD-2
Merge
wt
unc-10(md1117)
rab-3(js49)
Unc-10(md1117); rab-3(js49)
B
UNC-104/SYD-2
ICQ
0.5
0.4
0.3
0.2
0.1
0.0
****
****
****
wt
md1117
js49
md1117;js49
D
UNC-104/SYD-2 BiFC
Fluorescent Intensity (A.U.)
150000
100000
50000
0
****
****
wt
md1117
js49
C
UNC-104/UNC-104 BiFC
UNC-104/empty BiFC
P
A
wt
UNC-104/SYD-2 BiFC
unc-10(md1117)
rab-3(js49)

FIGURE 3

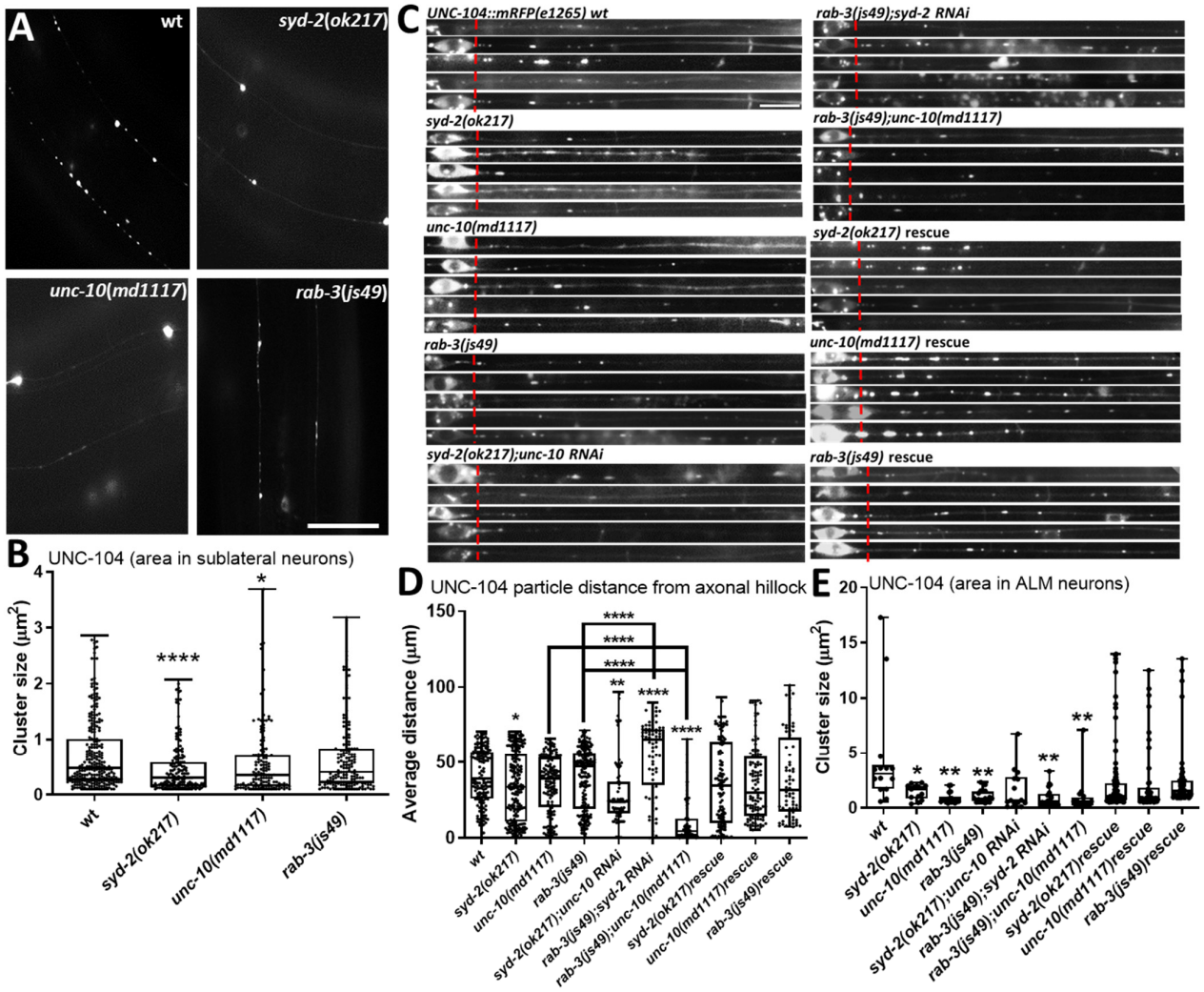
A
wt
syd-2(ok217)
unc-10(md1117)
rab-3(js49)
B
UNCC-104 (area in sublateral neurons)
Cluster size (µm²)
wt
syd-2(ok217)
unc-10(md1117)
rab-3(js49)
C
UNC-104::mRFP(e1265) wt
syd-2(ok217)
unc-10(md1117)
rab-3(js49)
syd-2(ok217);unc-10 RNAi
rab-3(js49);syd-2 RNAi
rab-3(js49);unc-10(md1117)
syd-2(ok217) rescue
unc-10(md1117) rescue
rab-3(js49) rescue
D
UNC-104 particle distance from axonal hillock
Average distance (µm)
wt
syd-2(ok217)
unc-10(md1117)
rab-3(js49)
syd-2(ok217);unc-10 RNAi
rab-3(js49);syd-2 RNAi
rab-3(js49);unc-10(md1117)
syd-2(ok217)rescue
unc-10(md1117)rescue
rab-3(js49)rescue
E
UNC-104 (area in ALM neurons)
Cluster size (µm²)
wt
syd-2(ok217)
unc-10(md1117)
rab-3(js49)
syd-2(ok217);unc-10 RNAi
rab-3(js49);syd-2 RNAi
rab-3(js49);unc-10(md1117)
syd-2(ok217)rescue
unc-10(md1117)rescue
rab-3(js49)rescue

FIGURE 4

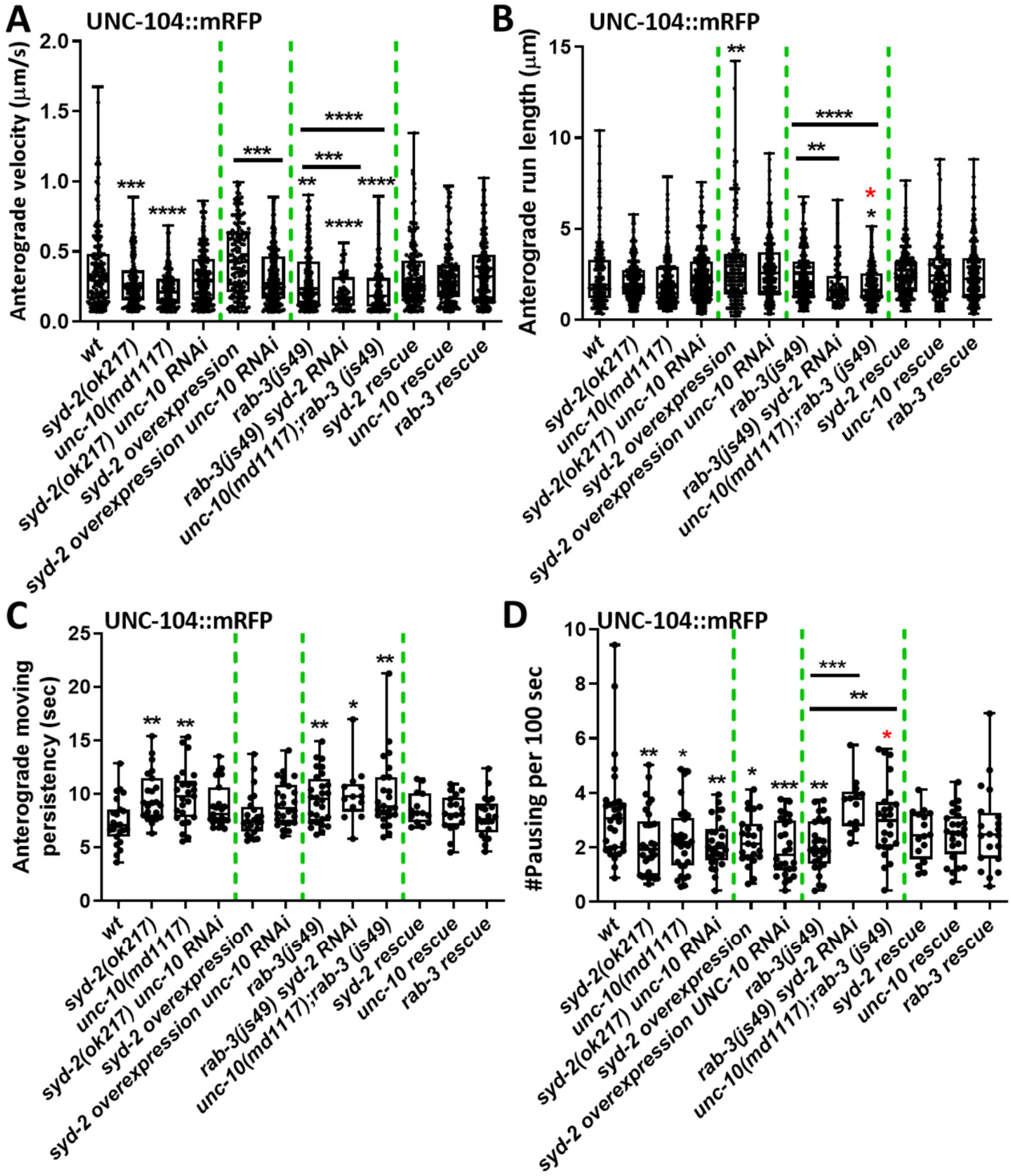
A
UNC-104::mRFP
Anterograde velocity (μm/s)
2.0
1.5
1.0
0.5
0.0
***
****
***
***
****
**
****
****
wt
syd-2(ok217)
unc-10(md1117)
syd-2(ok217) unc-10 RNAi
syd-2 overexpression
syd-2 overexpression unc-10 RNAi
rab-3(js49)
rab-3(js49) syd-2 RNAi
unc-10(md1117);rab-3 (js49)
syd-2 rescue
unc-10 rescue
rab-3 rescue
B
UNC-104::mRFP
Anterograde run length (μm)
15
10
5
0
**
****
**
*
*
C
UNC-104::mRFP
Anterograde moving persistency (sec)
25
20
15
10
5
0
**
**
**
*
**
D
UNC-104::mRFP
#Pausing per 100 sec
10
8
6
4
2
0
***
**
**
*
*
***
**
*
syd-2 overexpression UNC-10 RNAi

FIGURE 5

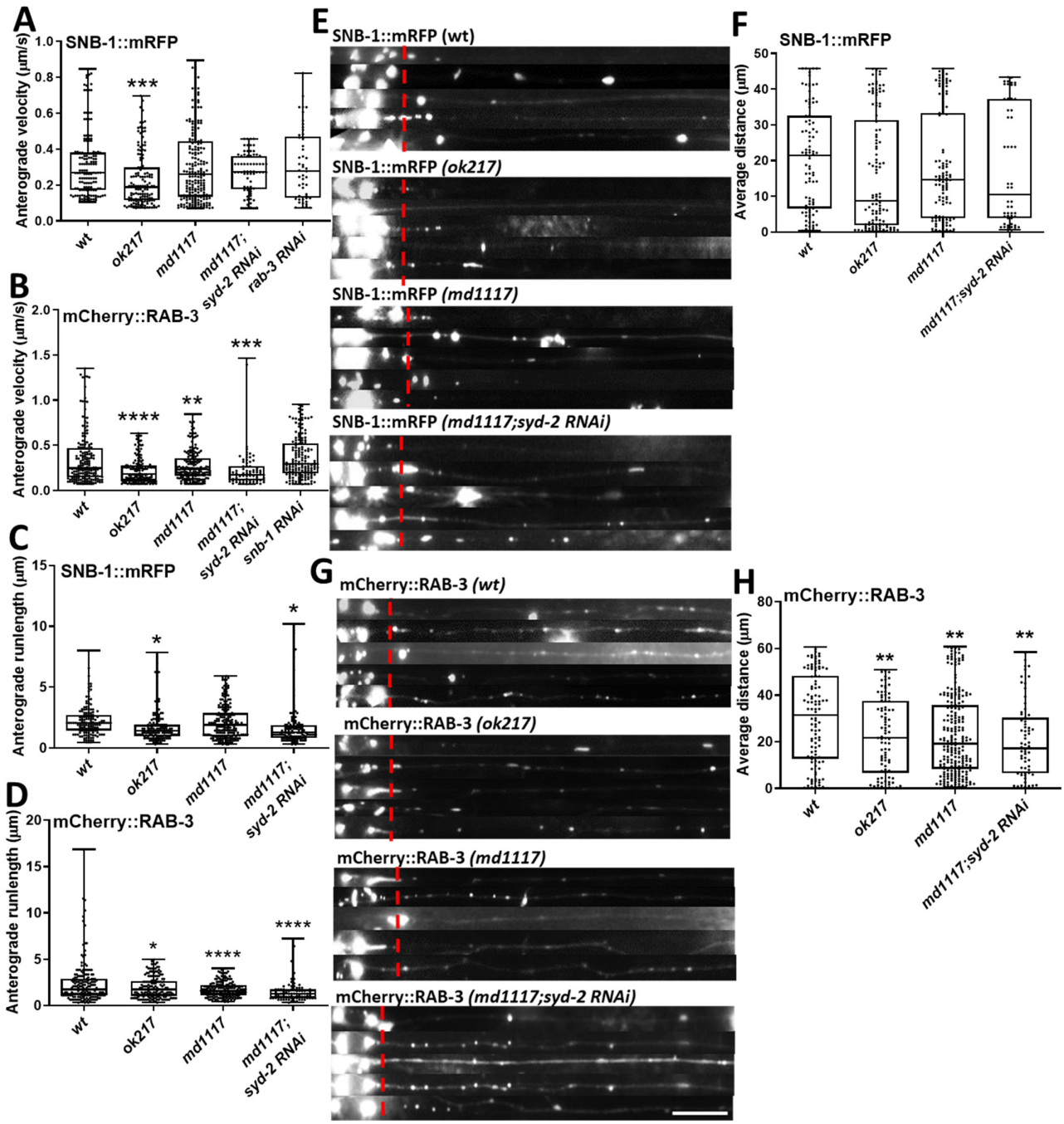
A
SNB-1::mRFP
Anterograde velocity (µm/s)
1.0
0.8
0.6
0.4
0.2
0.0
***
wt
ok217
md1117
md1117; syd-2 RNAi
rab-3 RNAi
B
mCherry::RAB-3
Anterograde velocity (µm/s)
2.0
1.5
1.0
0.5
0.0
****
**
***
wt
ok217
md1117
md1117; syd-2 RNAi
snb-1 RNAi
C
SNB-1::mRFP
Anterograde runlength (µm)
15
10
5
0
*
*
wt
ok217
md1117
md1117; syd-2 RNAi
D
mCherry::RAB-3
Anterograde runlength (µm)
20
15
10
5
0
*
****
****
wt
ok217
md1117
md1117; syd-2 RNAi
E
SNB-1::mRFP (wt)
SNB-1::mRFP (ok217)
SNB-1::mRFP (md1117)
SNB-1::mRFP (md1117;syd-2 RNAi)
F
SNB-1::mRFP
Average distance (µm)
50
40
30
20
10
0
wt
ok217
md1117
md1117;syd-2 RNAi
G
mCherry::RAB-3 (wt)
mCherry::RAB-3 (ok217)
mCherry::RAB-3 (md1117)
mCherry::RAB-3 (md1117;syd-2 RNAi)
H
mCherry::RAB-3
Average distance (µm)
80
60
40
20
0
**
**
**
wt
ok217
md1117
md1117;syd-2 RNAi

FIGURE 6

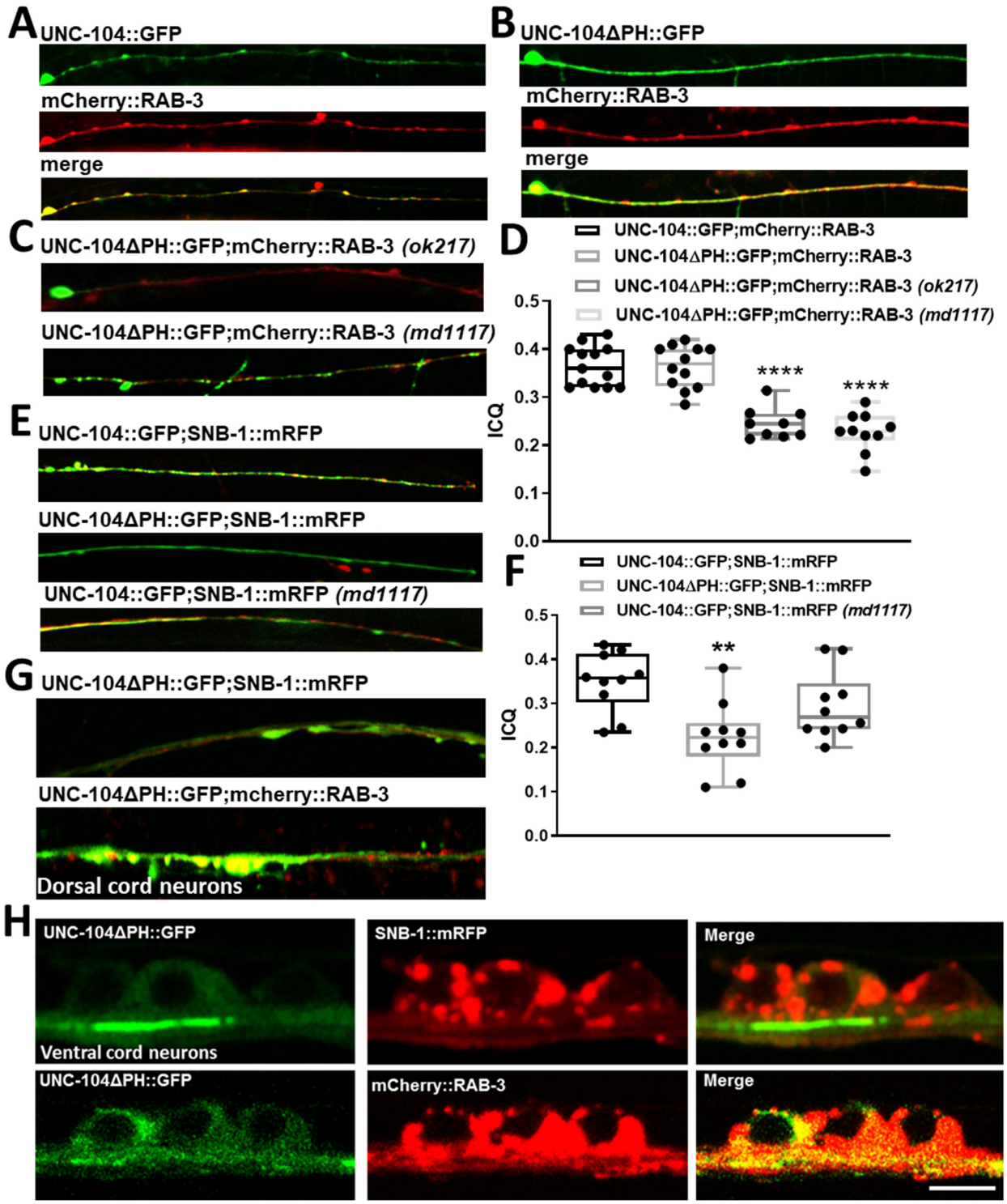
A
UNC-104::GFP
mCherry::RAB-3
merge
B
UNC-104ΔPH::GFP
mCherry::RAB-3
merge
C
UNC-104ΔPH::GFP;mCherry::RAB-3 (ok217)
UNC-104ΔPH::GFP;mCherry::RAB-3 (md1117)
D
UNC-104::GFP;mCherry::RAB-3
UNC-104ΔPH::GFP;mCherry::RAB-3
UNC-104ΔPH::GFP;mCherry::RAB-3 (ok217)
UNC-104ΔPH::GFP;mCherry::RAB-3 (md1117)
ICQ
0.5
0.4
0.3
0.2
0.1
0.0
****
****
E
UNC-104::GFP;SNB-1::mRFP
UNC-104ΔPH::GFP;SNB-1::mRFP
UNC-104::GFP;SNB-1::mRFP (md1117)
F
UNC-104::GFP;SNB-1::mRFP
UNC-104ΔPH::GFP;SNB-1::mRFP
UNC-104::GFP;SNB-1::mRFP (md1117)
ICQ
0.5
0.4
0.3
0.2
0.1
0.0
**
G
UNC-104ΔPH::GFP;SNB-1::mRFP
UNC-104ΔPH::GFP;mcherry::RAB-3
Dorsal cord neurons
H
UNC-104ΔPH::GFP
SNB-1::mRFP
Merge
Ventral cord neurons
UNC-104ΔPH::GFP
mCherry::RAB-3
Merge

FIGURE 7

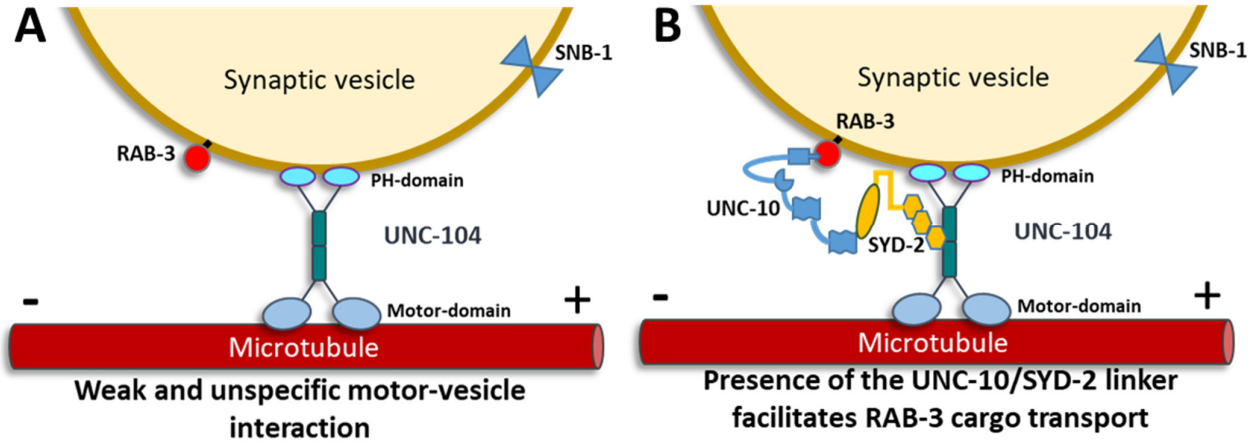
A
Synaptic vesicle
SNB-1
RAB-3
PH-domain
UNC-104
-
+
Motor-domain
Microtubule
Weak and unspecific motor-vesicle interaction
B
Synaptic vesicle
SNB-1
RAB-3
PH-domain
UNC-10
SYD-2
UNC-104
-
+
Motor-domain
Microtubule
Presence of the UNC-10/SYD-2 linker facilitates RAB-3 cargo transport

SUPPLEMENTARY MATERIAL

SUPPLEMENTARY FIGURE LEGENDS

Suppl. Figure S1: (A) Simplified scheme of the nervous system of *C. elegans*. Employed neurons and nervous structures for this study are highlighted in red. The nerve ring is a large ganglion hosting hundreds of neurons and is the so called "brain" of the worm. (B) Schematic domain structures of UNC-104, UNC-10, SYD-2 and RAB-3 with used alleles in this study highlighted in red. (C) Cartoon explaining the determination of a particle's average travel distance in axons. (D) Kymograph representing various motility parameters. Vertical scale bar: 25 sec and horizontal scale bar: 10 µm

Suppl. Figure S2: (A) Frequency distribution of UNC-104 anterograde velocities (from Figure 4A). (B) Frequency distribution of UNC-104 anterograde run lengths (from Figure 4B).

Suppl. Figure S3: (A-D) Line scans along neurons in images as displayed in Figure 6A-C.

Suppl. Figure S4: (A-D) Line scans along neurons in images as displayed in Figure 6E.

SUPPLEMENTARY FIGURES

SUPPLEMENTARY FIGURE S1

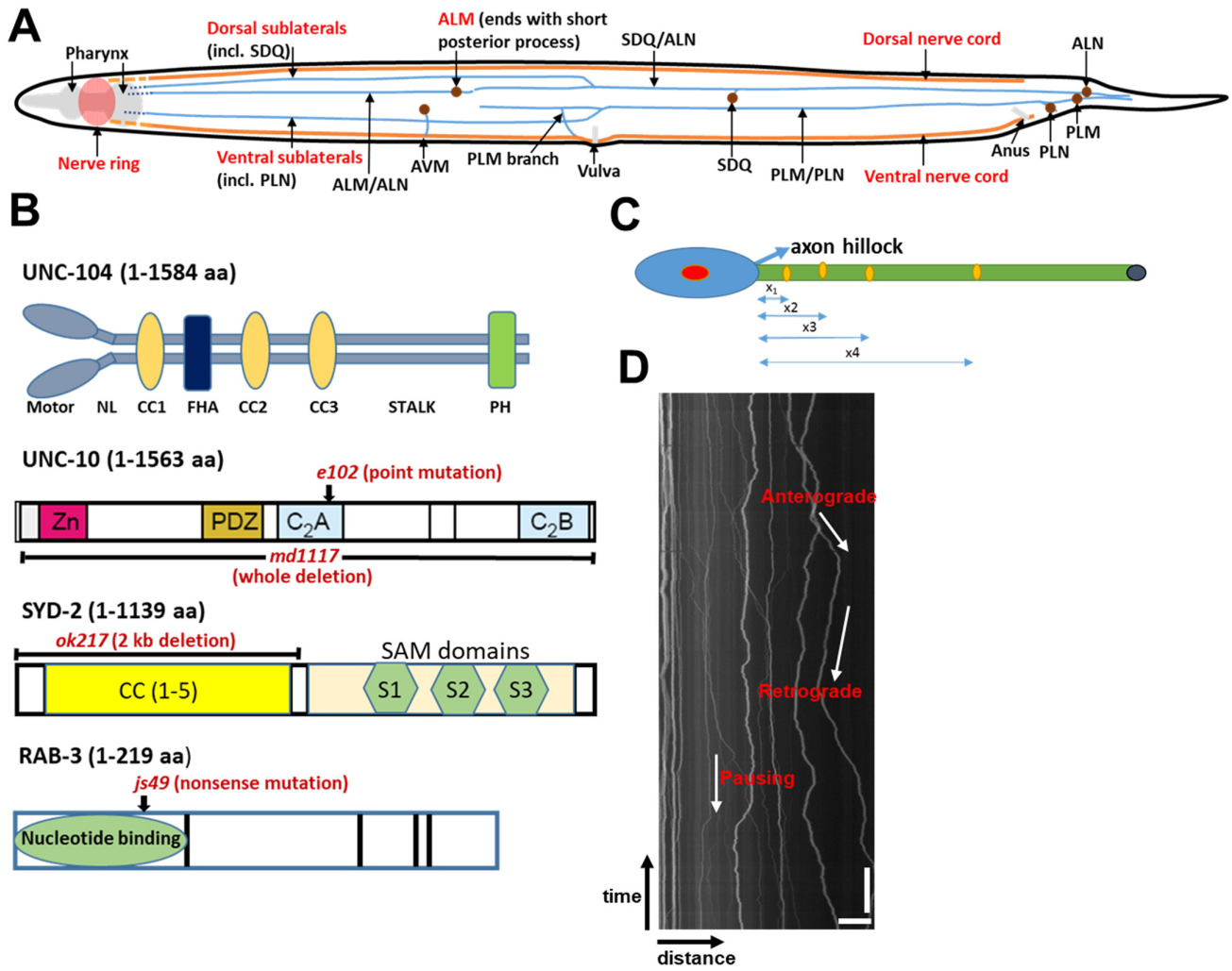

SUPPLEMENTARY FIGURE S2

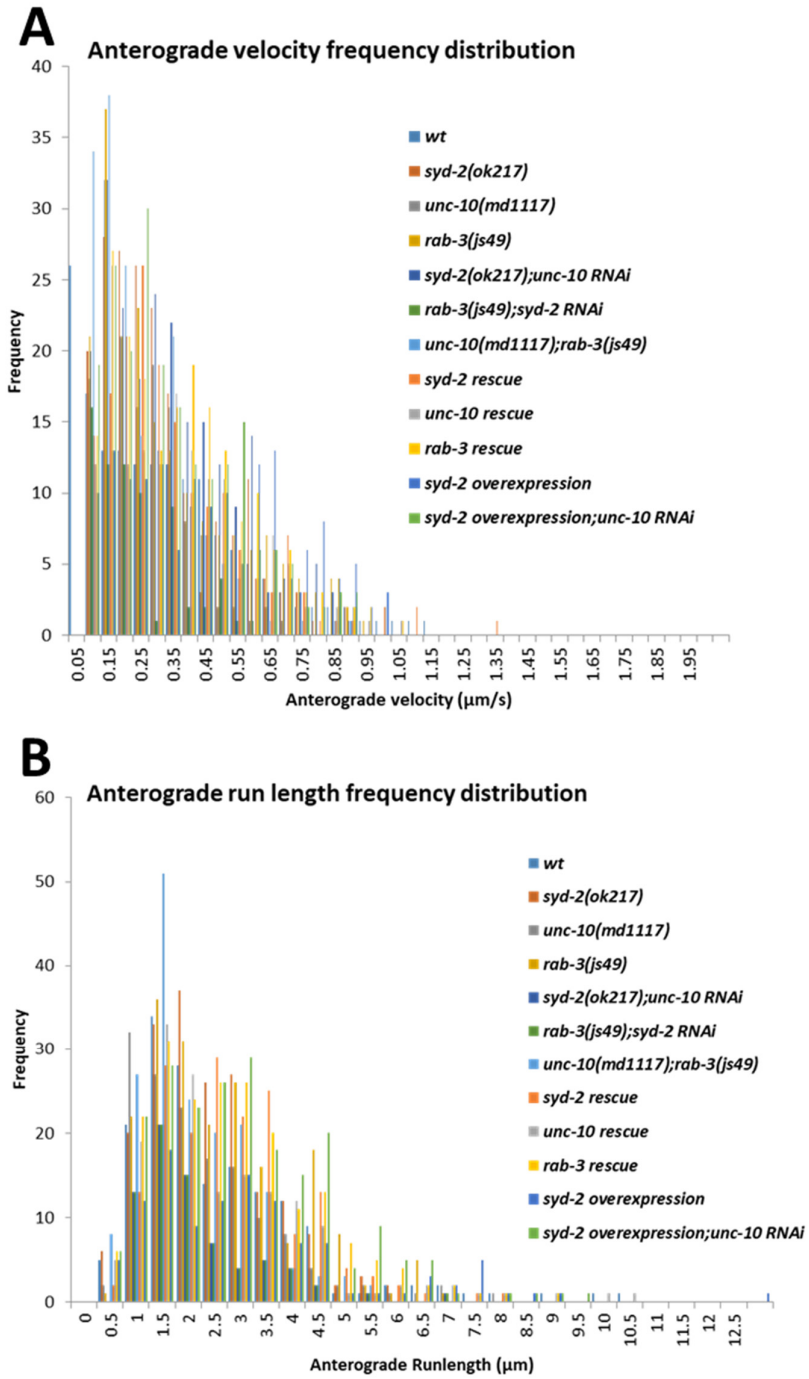

SUPPLEMENTARY FIGURE S3

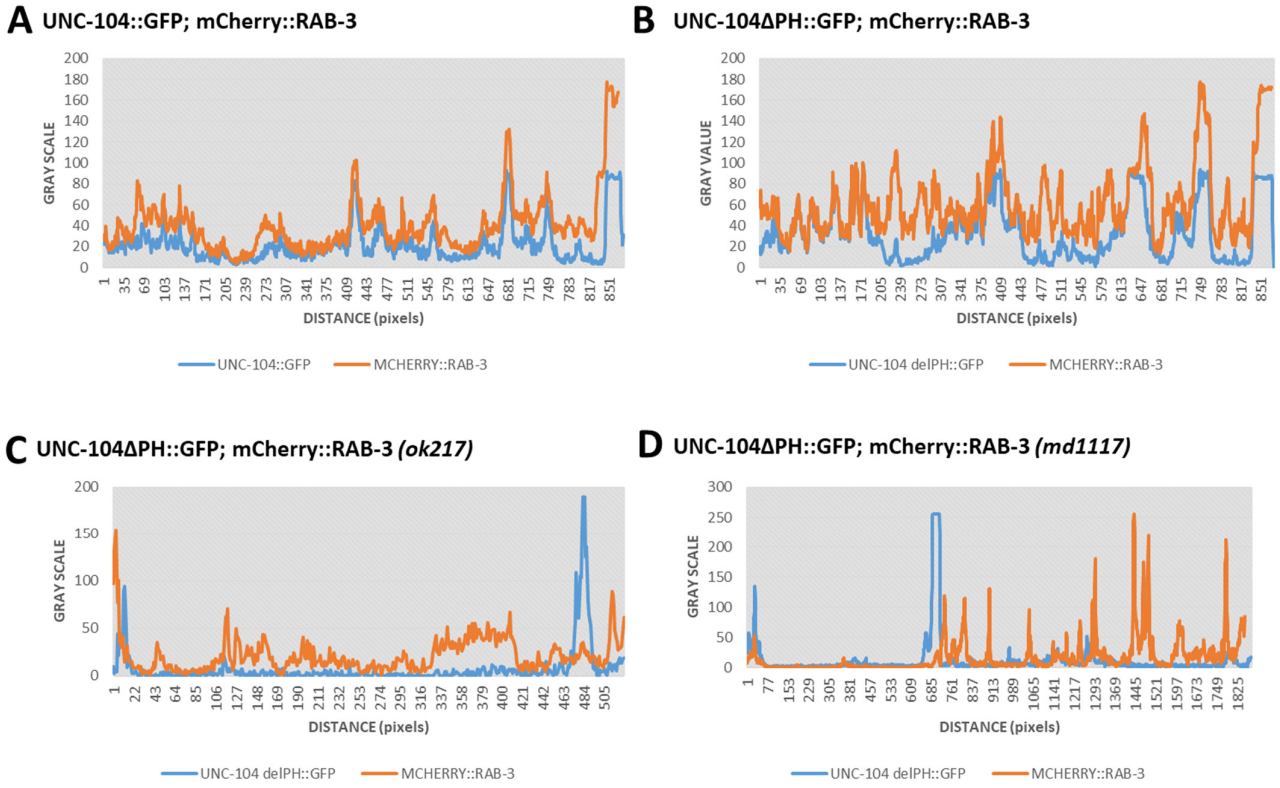

SUPPLEMENTARY FIGURE S4

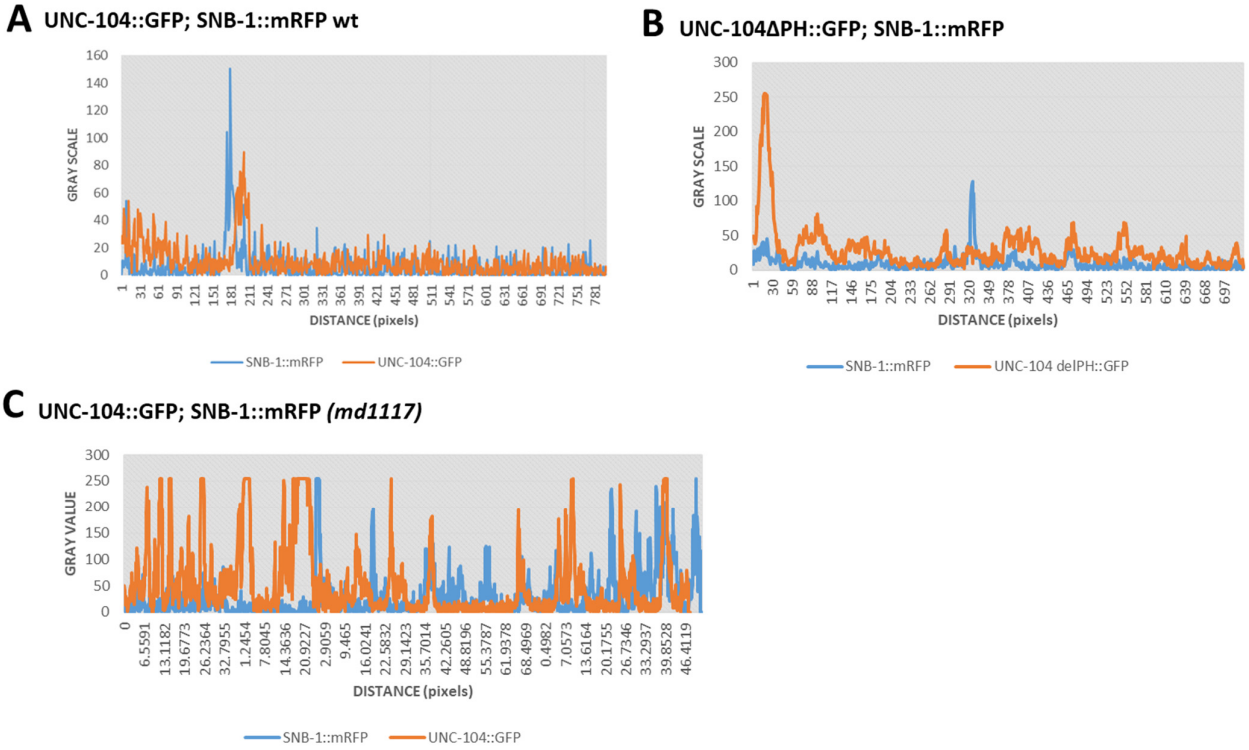

SUPPLEMENTARY TABLE LEGENDS

Supplementary Table S1: Accompanying table with details to Figure 3B.

Supplementary Table S2: Accompanying table with details to Figure 3D+E.

Supplementary Table S3: Accompanying table with details to Figure 4A+B.

Supplementary Table S4: Accompanying table with details to Figure 4C+D.

Supplementary Table S5: Accompanying table with details to Figure 5A-D.

Supplementary Table S6: Accompanying table with details to Figure 5F+H.

SUPPLEMENTARY TABLES

Suppl. Table S1

UNC-104 ::mRFP	wt	*syd-2 (ok217)*	*unc-10 (md1117)*	*rab-3 (js49)*
Average cluster size (μm^2)	0.72±0.64	0.474±0.38	0.574±0.48	0.655±0.56
Total neurite length (mm)	1.95	2.44	1.44	1.28
Cluster per 100 µm	19.55	15.5	22.7	25.4
# cluster	382	380	330	326

Suppl. Table S2

	Average distance (µm)	Cluster size (μm^2)
UNC-104::mRFP	Mean±SEM	Mean±SEM
wt	40.77±1.510	4.458±1.253
syd-2(ok217)	34.26±1.563	1.445±0.189
unc-10(md1117)	35.60±1.602	0.883±0.119
rab-3(js49)	39.63±1.432	1.021±0.413
syd-2(ok217);unc-10 RNAi	29.30±2.442	1.702±0.502
rab-3(js49);syd-2 RNAi	54.41±2.866	0.898±0.177
rab-3(js49);unc-10(md1117)	9.809±1.255	0.976±0.420
syd-2 rescue	35.99±2.472	2.522±0.383
unc-10 rescue	36.07±2.346	2.304±0.486
rab-3 rescue	40.01±3.316	2.599±0.458

Suppl. Table S3

	Anterograde velocity (µm/s)			Anterograde run length (µm)	
UNC-104::mRFP	Mean	SEM	N	Mean	SEM
wt	0.378	0.021	165	2.430	0.137
syd-2(ok217)	0.280	0.012	193	2.203	0.082
unc-10(md1117)	0.230	0.010	155	2.139	0.113
rab-3(js49)	0.306	0.015	194	2.483	0.098
syd-2(ok217);unc-10 RNAi	0.321	0.012	223	2.487	0.098
rab-3(js49);syd-2 RNAi	0.214	0.015	170	1.936	0.130
rab-3(js49);unc-10(md1117)	0.224	0.011	172	1.863	0.076
Syd-2 overexpression	0.438	0.020	155	3.021	0.183
Syd-2 overexpression;unc-10 RNAi	0.321	0.013	207	2.792	0.114
syd-2 rescue	0.331	0.016	175	2.563	0.099
unc-10 rescue	0.327	0.016	161	2.679	0.128
rab-3 rescue	0.353	0.015	202	2.590	0.110

Suppl. Table S4

	Anterograde persistency (sec)		Pausing per 100 sec	
UNC-104::mRFP	Mean	SEM	Mean	SEM
wt	7.425	0.459	3.257	0.333
syd-2(ok217)	9.727	0.484	2.179	0.220
unc-10(md1117)	9.830	0.521	2.264	0.220
rab-3(js49)	9.607	0.448	2.067	0.175
syd-2(ok217);unc-10 RNAi	8.925	0.430	2.150	0.165
rab-3(js49);syd-2 RNAi	9.982	0.727	3.570	0.263
rab-3(js49);unc-10(md1117)	9.982	0.693	3.008	0.279
Syd-2 overexpression	7.969	0.425	2.288	0.190
Syd-2 overexpression;unc-10 RNAi	9.112	0.401	1.978	0.199
syd-2 rescue	8.642	0.402	2.449	0.231
unc-10 rescue	8.230	0.405	2.486	0.190
rab-3 rescue	7.886	0.412	2.658	0..339

Suppl. Table S5

	Anterograde velocity (µm/s)			Anterograde run length (µm)	
SNB-1::mRFP	Mean	SEM	N	Mean	SEM
wt	0.317	0.015	158	2.243	0.106
syd-2(ok217)	0.230	0.012	159	1.798	0.115
unc-10(md1117)	0.315	0.014	203	2.411	0.123
unc-10(md1117);syd-2 RNAi	0.270	0.012	72	1.837	0.160
rab-3 RNAi	0.3104	0.028	149	n/a	n/a
mCherry::RAB-3					
wt	0.351	0.021	174	2.451	0.170
syd-2(ok217)	0.226	0.011	158	1.970	0.092
unc-10(md1117)	0.275	0.012	182	1.768	0.064
unc-10(md1117);syd-2 RNAi	0.233	0.026	74	1.527	0.132
snb-1 RNAi	0.367	0.018	184	n/a	n/a

Suppl. Table S6

	SNB-1::mRFP	mCherry::RAB-3
	Average distance (µm)	Average distance (µm)
wt	20.49±1.503	29.93±1.839
syd-2(ok217)	16.13±1.507	22.41±1.706
unc-10(md1117)	18.03±1.431	22.81±1.142
unc-10(md1117);syd-2 RNAi	18.16±2.290	20.38±1.986